Distribution and sea-to-air exchange of carbon monoxide in surface microlayer and subsurface seawater in the eastern marginal seas of China

Lin Yang [a, b], Bin Yang [a], Jing Zhang [b, c, *], Anja Engel [d], Gui-Peng Yang [b, c, *]

[a] *Jiangsu Key Laboratory of Marine Bioresources and Environment, Jiangsu Ocean University, Lianyungang, 222005, China*

[b] *Frontiers Science Center for Deep Ocean Multispheres and Earth System, and Key Laboratory of Marine Chemistry Theory and Technology, Ministry of Education, Ocean University of China, Qingdao 266100, China*

[c] *Laboratory for Marine Ecology and Environmental Science, Qingdao National Laboratory for Marine Science and Technology, Qingdao 266237, China*

[d] *GEOMAR Helmholtz Centre for Ocean Research, 24105 Kiel, Germany*

*Corresponding author:

E-mail address: zhangjouc@ouc.edu.cn (J. Zhang); gpyang@mail.ouc.edu.cn (G.P. Yang)

Keywords: Carbon monoxide; Enrichment Factors; Surface microlayer; Sea-to-air flux; Photoproduction; Bacterial consumption; Eastern marginal seas of China

Abstract

* Corresponding authors. Key Laboratory of Marine Chemistry Theory and Technology, Ministry of Education, Ocean University of China, Qingdao 266100, China
E-mail addresses: zhangjouc@ouc.edu.cn (J. Zhang); gpyang@mail.ouc.edu.cn (G.P. Yang)

Sea-surface microlayer (SML) is the boundary interface between the atmosphere and ocean, exhibiting an enrichment of dissolved organic matter (DOM) and participating in sea-to-air gas exchange. However, how DOM enrichment in the SML controls the flux of several gases in sea-to-air exchange remains poorly understood. In our study, incubation experiments and in-situ investigation in the eastern marginal seas of China were conducted to determine the distribution of carbon monoxide (CO) and its production and consumption rates in the SML during winter. Chromophoric DOM (CDOM) (92%) and fluorescent DOM (FDOM) (92%) were frequently enriched in the SML during winter, and the enrichment of CO was lower than the enrichments of CDOM and FDOM. CO ranged from 0.48 to 2.81 nmol L^{-1} (1.22 ± 0.85 nmol L^{-1}) and 0.50 to 3.61 nmol L^{-1} (1.54 ± 1.61 nmol L^{-1}) in the subsurface layer (SSW) and the SML, respectively, with higher concentration observed in the SML due to CDOM enrichment. Enrichment in the SML was expressed as enrichment factors (EFs) defined as the ratio of values in the SML to those in the SSW. Although CO, CDOM and FDOM concentrations decreased from in-shore regions to open oceans, higher enrichment factors (EFs > 2) of CO and DOM in the SML were generally observed in the off-shore areas. Considering the photoproduction rate (mean value: 12.41 nmol L^{-1} d^{-1}) of CO in the SML was significantly higher than that in the SSW (10.32 nmol L^{-1} d^{-1}), the enrichment and the concentration of CO in the SML showed a diurnal variation, with the higher values observed in the early afternoon. The flux of CO exhibited a significantly negative correlation with the CDOM absorption coefficient at 254 nm and marine-humic-like FDOM in the SML, suggesting that elevated DOM could stimulate the photoproduction of CO, but may also decrease sea-to-air CO exchange in the SML. Given the importance of

the organic-rich SML as a diffusion layer in the air–sea exchange of climate-relevant gases and heat, understanding the layer's enrichment processes is crucial.

1. Introduction

Carbon monoxide (CO) is an indirect greenhouse gas, and it plays an important role in atmospheric chemistry (Nguyen et al., 2020). It is the predominant sink of hydroxyl radical (OH•, Conte et al., 2019; Cordero et al., 2019), which oxidizes pollutants and greenhouse gases (such as CH_4) emitted to the atmosphere by human activities (Nguyen et al., 2020). The photodegradation of dissolved organic matter (DOM) is thought to be the main source of CO in the ocean (Stubbins et al., 2006), and the ocean acts as a source of atmospheric CO (Mopper and Kieber, 2002). In addition, direct production of CO by phytoplankton has been observed in laboratory experiments (Troxler et al., 1972; Gros et al., 2009) and dark/thermal production was also inferred from modeling at Bermuda Atlantic Time Series (BATS, Kettle, 2005), and from incubations of water samples from the Delaware Bay (Xie et al., 2005) and St Lawrence estuary (Zhang et al., 2008). Microbial consumption and the sea-to-air fluxes (Doney et al., 1995; Song et al., 2015) of CO are considered to be the main sinks of oceanic CO (Zafiriou et al., 2003). The average annual sea-to-air flux accounted for 10% of the global CO sinks estimated by Zafiriou et al. (2003), Conte et al. (2019) and Yang et al. (2024). In the ocean, CO acts as a microbial energy source that supports food webs, a link in carbon cycling that connects surface and deep waters, and a modulator of oxygen cycles. With increasing concern about atmospheric pollution and the potential role of

CO, a primary goal of studying oceanic CO concentrations is to evaluate its long-term stability and distribution trends in the marine boundary layer (Conte et al., 2019; Xu et al., 2023), where the ocean and atmosphere exchange momentum, heat, moisture, and gases.

The ocean surface layer plays a vital role in climate change through the sea-to-air exchange of greenhouse gases. The sea-surface microlayer (SML) is located at the sea-to-air interface and is considered to play a critical role in global biogeochemical cycles and climate change by regulating the sea-to-air exchange of gases and aerosol particles (Liss and Duce, 1997; Cunliffe et al., 2013). In addition, SML is exposed to the most intense solar radiation of any seawater layer, especially ultraviolet (UV) light, and shows significantly higher colored dissolved organic matter (CDOM) concentration and microbial abundances compared to the subsurface layer (SSW, Obernosterer et al., 2006; Obernosterer et al., 2008; Wurl et al., 2009; Yang et al., 2022). For decades, articles have emphasized the presence and enrichment of organic matter and gases (CO and DMS) in the SML (Liss and Duce, 1997; Orellana et al., 2011; Ma and Yang, 2023; Sugai et al., 2020), but it remains unclear how this is maintained whilst CO is lost to the atmosphere.

Generally, the sea-to-air flux is estimated from CO concentration in surface waters (2 to 10 m), but there is evidence that biogeochemical processes within the SML may also affect the CO flux (Sugai et al., 2020). CDOM and surfactant enrichment in the SML relative to the SSW has been reported, with an enrichment factor (EF) range of 0.4 to 6.7 (Huang et al., 2015; Shaharom et al., 2018; Yang et al., 2022), and mediates

all mass transfer across the SML (Rickard et al., 2019 and 2022). Although intense solar radiation and enrichment of DOM may promote CO photoproduction involving SML (Cunliffe et al., 2013; Pereira et al., 2018; Sugai et al., 2021), and likely modify sea-to-air gas transfer velocity (k_w) of CO and other gases (Pereira et al., 2018). The role and response of the SML, along with the complex interplay of biological, geochemical, and physical processes, govern the transfer of CO from the SSW, where it can either be consumed by bacteria or released into the atmosphere. Our study hypothesized that SML-specific environmental changes (i.e., enrichment processes and biogeochemical processes) and the abundance and composition of DOM in the eastern marginal seas of China influence the rate of sea-to-air CO exchange, and they contribute to the formation of the marine boundary layer involved in atmospheric chemistry and climate regulation.

2. Materials and Methods

2.1 Study Area

The Yellow Sea (YS) and the East China Sea (ECS) are marginal seas of the western Pacific Ocean with complicated hydrological characteristics and are substantially affected by the Yellow Sea Cold Water Mass (YSCWM), the Kuroshio Current, and the coastal currents (Fig. 1). The YSCWM is a low-temperature (< 10°C) and high-salinity (32.0–33.0) water mass. Seawater in the Kuroshio presents high temperatures (20–29°C), high salinities (34.2–34.8), and low suspended particulate concentrations (SPC) (< 2 mg L^{-1}) (Yang et al., 2022). The Changjiang River contributed more than 80% of the total freshwater inflow to the YS and the ECS

(Wang et al., 2020). In addition, the atmospheric circulation in the study area was generally governed by the East Asian monsoon, with strong northerly winds prevailing from September to April. Low pressure over the northwestern Pacific Ocean produced offshore winds that transported continental air masses into the study area (Li et al., 2019). This interaction significantly influences the hydrological conditions, circulation structures, material exchange, ecological environment, and the biogeochemical processes of CO and DOM in the region (Chen, 2009; Yu et al., 2025; Zhang et al., 2007).

2.2 Sampling and analysis

We collected 52 paired SML and SSW water samples in the YS and ECS aboard the R/V "*Dong Fang Hong 3*" from 28 December 2019 to 16 January 2020. There were 38 sampling stations during the daytime (7:00-19: 00) and 32 sampling stations during the nighttime (19:00-7: 00). SSW samples were collected at 2–5 m depth using 24 × 10 L Niskin bottles mounted on a rosette equipped with a conductivity–temperature–depth (CTD) profiler. SML sampling used a Garrett Screen (Garrett, 1965; Chen et al., 2016; Ma and Yang, 2023) (mesh: 16 mm, wire diameter: 0.36 μm; effective surface area: 2.025 cm^2) according to standard procedures (Pereira et al., 2016; Sabbaghzadeh et al., 2017) when seawater conditions were calm. While SML integrity is disrupted by a moving vessel, or when sampling from its stern (Cunliffe and Wurl, 2014; Wurl et al., 2016), the SML can be successfully sampled from a vessel's bow while on-station (Sabbaghzadeh et al., 2017) with the ambient waterflow toward the RV (Cunliffe and

Wurl, 2014). The sampling distance is at a certain distance (5 ~ 8 m) where the CTD sampler was deployed, and both SSW and SML CO did not change during the sampling. We therefore adopted this procedure, hand-deploying the Garrett Screen over the bow on the crest of a wave (Cunliffe and Wurl, 2014) and further minimizing potential contamination (engines off, wheelhouse and afterdeck downwind) (Pereira et al., 2016).

A TA3000R trace gas analyzer (Ametek, USA) was used to measure CO concentrations in the atmosphere and seawater with a lower detection limit of 10 ppbv. Before analysis, the instrument was calibrated using a CO standard gas (nominal concentration: 100 ppbv in zero-grade air; analytical accuracy: ± 2%, State Center for Standard Matter, China). The calibration was repeated every six hours during measurements. Atmospheric CO samples ($[CO]_{atm}$, ppbv) were collected about 10 m above sea level using a 10 mL gas-tight syringe (VICI, USA) and were obtained by injecting atmospheric samples directly into the instrument through a PTFE hydrophobic filter membrane (Millipore, USA, atmospheric CO samples were filtered for dust/aerosol particles) into the TA3000R trace gas analyzer for determination. To minimize the influence of ship emissions, $[CO]_{atm}$ samples were collected from the highest deck of the ship (~10 m), facing the wind, with 8 mL gastight glass syringes when the ship was decelerating. CO in seawater was measured using the headspace equilibrium method (Xie et al., 2002), wherein a 50 mL sample bottle was filled with seawater sample and sealed (as above), and then an equivalent amount of the seawater sample was replaced with 8 mL of ultrahigh-purity N_2 using a gas-tight syringe. The samples were then shaken at 300 r min^{-1} for 5 min to ensure that the nitrogen-filled

149 headspace in the bottle reached gas-liquid equilibrium before 6 mL of the equilibrated
150 gas was extracted using a gas-tight syringe and injected through a PTFE hydrophobic
151 filter membrane (Millipore, USA) into the TA3000R trace gas analyzer for
152 determination (the PTFE filter membranes were set up to prevent the potential entry of
153 liquid water). The measured equilibrated headspace mixing ratio of CO (ppbv) was
154 corrected using the saturated water vapor pressure and standard atmospheric pressure
155 (Stubbins et al., 2006) and then converted to obtain the concentration of dissolved CO
156 (nmol L^{-1}) in seawater. The method's lower detection limit was 0.02 nmol L^{-1}, with an
157 analytical accuracy of better than 10%.

158 The SML samples were collected in 500 mL brown sample bottles. The screen
159 was held level and dipped into the sea surface, moved laterally to sample from an
160 undisturbed film, and then withdrawn slowly from the surface. Repeated dipping (11
161 times, 600 mL) was conducted until the desired volume was collected (the depths of
162 the SML samples ranged within 100–500 μm, Garrett, 1965). The screening method is
163 often applied during field studies because of its relative quickness and large sample
164 volume compared to other techniques (Chen et al., 2016). CO in seawater samples was
165 collected and measured first on board, immediately after collection. A comparison
166 showed that screen-collected samples usually exhibit greater microlayer enrichment of
167 gas than the plate-collected samples, indicating that the screen sampler might be more
168 effective for in-situ measurements (Yang et al., 2001). CDOM, DOC, and Chl-*a*
169 samples were filtered using 0.7 μm glass fiber filters (GF/F, Whatmann) and the
170 filtrates were transferred to 60- and 40-mL brown glass bottles (pre-cleaned and pre-

combusted) for later CDOM and DOC analyses. All samples were frozen (−20°C) and protected from light. Upon arriving at the land laboratory, samples were analyzed as soon as possible. Sea-surface temperature and salinity were obtained from the sensors on the Seabird 911 CTD rosette. Seawater temperature and salinity in the SML were measured *in situ* using a pre-calibrated multi-parameter water quality probe (AP-5000, Aquaread Co., UK). Meteorological data (e.g., wind speed and air temperature, ~ 10 m) were recorded simultaneously by a ship-borne weather instrument (Li et al., 2019, Table S1). Net solar radiation is the balance between all incoming and outgoing radiant energy fluxes at the Earth's surface. Our ocean surface net solar radiation was measured and recorded using a net radiometer (Table S1). Ocean surface net solar radiation is significant in research on the Earth's heat balance systems, sea-to-air interactions, and other applications.

2.3 Photoexposure experiments

The in-situ natural sunlight incubation experiment was conducted to estimate the CO photoproduction rates in different seawater layers. SSW and SML samples for photochemical incubation were collected from stations B1 and C4, as well as E2, FJ5, P1, and P7, located in the YS and the ECS, respectively (Fig. 1). SML and SSW (5 m below seawater surface) samples (SSW: 2 L; SML: 500 mL) were passed through a 0.22 μm PES filters (Pall Corp. Port Washington, NY, USA) immediately to remove the majority of the bacteria and was then placed in an acid-washed and pre-combusted quartz tubes (120 mL, acid-washed and pre-combusted) in a natural sunlight incubation

and sealed without headspace or air bubbles. Photo incubation experiments were conducted on the ship immediately after sample collection. To measure the photoproduction at solar radiation production rates of CO, the quartz tubes were treated as follows: (1) uncovered quartz tubes exposed to full-spectrum irradiation; (2) quartz tubes wrapped in multiple layers of aluminum foil to eliminate all light transmission. Treatment (2) was subtracted from light-exposed treatments to remove the fraction of CO produced by dark production. The quartz tubes were positioned under the in-situ irradiation source to maximize the exposure of the sample; the water depth in each tube was 5 cm (i.e., the diameter of the tube). SML and SSW quartz tubes were irradiated for 4 hours and were exposed to direct solar irradiation while being held in a water bath with circulating seawater. The change in the CO photoproduction with time can be seen as a constant due to the relatively small amount of total radiation during the short exposure time. The turnover time of the photochemical production (τ_{prod}) and biological consumption (τ_{cons}) in the SML (SSW) was calculated by the following equations (Doney et al., 1995; Jones and Amador, 1993):

$$\tau_{prod} = [CO] \text{ in SML} / \text{photochemical CO production rate in SML} \quad (1)$$

$$\tau_{cons} = 1/k_{CO} \text{ in SML} \quad (2)$$

2.4 Microbial consumption and dark production experiments

Six stations were selected to determine the microbial consumption rates of CO (YS: stations A1, B1, and C4; ECS: stations E2, T2, and S6). CO concentrations in seawater samples were measured immediately after collection from the SSW and the

SML and used as background values. Seawater was used to fill 1 L glass syringes equipped with a 3-way nylon valve, which were pre-cleaned with 10% HCl-Milli-Q water and Milli-Q water until free of headspace, and wrapped with aluminum foil. The syringes were immersed in a shallow tank of flowing water that was continuously pumped from the sea to maintain the temperature of the incubation experiments equal to that of the ambient surface seawater. Each sampling series consisted of 4–5 points, and the data from each series were fitted exponentially to determine the consumption rate constant (k_{bio}).

The dark production incubations were used to eliminate the effect of dark production from the microbial CO consumption measurements. According to Zhang et al. (2008), the dark production is the abiotic dark production. Seawater was first filtered through 0.2 μm polyethersulfone membranes and bubbled with CO-free gas (ultrahigh-purity N_2, China) to reduce the background CO values before being put into the 1 L syringes as previously described. Then syringes were rinsed with the sample water and then overflowed with the sample twice their volumes before they were closed without headspace. All incubations were conducted in duplicate, and wrapped in multiple layers of aluminum foil, and placed in the same incubator environment. Samples were collected at 0, 0.5, 1, 2, and 4 h during incubation. CO incubation experiment was performed under the same conditions as the CO degradation processes according to the method of Xie et al. (2005) and Xu et al. (2023).

2.5 Calculation of sea-to-air flux of CO

The two-layer model proposed by Liss and Merlivat (1986) was used to calculate the instantaneous sea-to-air flux of CO according to the following equation:

$$F = k([CO]_{surf} - [CO]_{eq}) \quad (3)$$

Where F refers to the sea-to-air flux of CO (nmol m^{-2} h^{-1}), and k is the gas transfer coefficient (cm h^{-1}) as a function of wind speed u (m s^{-1}) and the Schmidt number of CO (Sc). In this paper, we used empirical formula E2011 (Edson et al., 2011), which applies to wind speeds from 0 to 18 m s^{-1} (Wind speed ranged from 0.68 m s^{-1} to 12.00 m s^{-1}), to calculate the gas transfer coefficient as follows:

$$k = (0.029u^3 + 5.4)\,(Sc/660)^{-1/2} \quad (4)$$

The Schmidt number of CO was referenced from the research of Zafiriou et al. (2008):

$$Sc = -0.0553t^3 + 4.3825t^2 - 140.07t + 2134 \quad (5)$$

where t is seawater temperature (°C).

$[CO]_{surf}$ represents the concentration of CO in the initial SML and SSW seawater, calculated by the following equation:

$$[CO]_{surf} = pm_a\,(\beta pV_w + V_a)/(RTV_w) \quad (6)$$

Where *P* is the standard atmosphere pressure (atm) and *ma* represents the concentration of CO in the headspace when the sample reaches equilibrium. β is the Bunsen solubility coefficient which is dependent on salinity and temperature (Wiesenburg and Guinasso, 1979). *Vw* and *Va* are the volumes of seawater and headspace in the sample bottle,

254 respectively. *T* is temperature (in Kelvin) and *R* is the gas constant with the value of
255 0.08206 atm L (mol K)$^{-1}$.

256 The daily fluxes (μmol m^{-2} d^{-1}) of CO in the YS and the ECS were calculated
257 using the method reported by Stubbins et al. (2006) and Yang et al. (2011), based on
258 the hourly flux (μmol m^{-2} h^{-1}). These hourly fluxes were examined on the scale of
259 individual days by plotting hourly fluxes against the time of day. Days without full
260 coverage of diurnal variations were discarded, leaving 4 days of data in the final
261 analysis. The area under each daily curve was calculated (OriginPro 8.0) to give daily
262 CO emissions.

263 *2.6 Determination of CDOM absorption*

264 The Napierian absorption coefficients of CDOM ($a_{CDOM}(\lambda)$ (m^{-1})) were calculated
265 as follows:

266 $$a_{CDOM}(\lambda) = 2.303\ A_{CDOM}(\lambda)/L \quad (7)$$

267 Where $A_{CDOM}(\lambda)$ is the absorbance of the sample at wavelength λ; and L is the cell
268 pathlength of the quartz cuvette in meters (0.1 m, Stedmon and Markager, 2003).
269 CDOM absorption $a_{CDOM}(254)$ is an effective proxy for dissolved organic carbon (DOC)
270 and chlorophyll-*a* (Chl-*a*) concentrations in the eastern marginal seas of China (Yang
271 et al., 2021).

272 The spectral slope of the absorption spectrum was obtained by nonlinear fitting of
273 the absorption coefficient according to the following equation (Stedmon and Markager,
274 2003):

$$a_{CDOM}(\lambda) = a_{CDOM}(\lambda_0)\exp[-S(\lambda - \lambda_0)] + K \quad (8)$$

Where $a_{CDOM}(\lambda)$ and $a_{CDOM}(\lambda_0)$ are the Napierian absorption coefficients at wavelengths λ and λ_0; λ_0 is the reference wavelength (440 nm); S is the spectral slope of the absorption spectrum; and K represents the background parameters with CDOM removed (Yang et al., 2022). The specific UV absorbance ($SUVA_{254}$) can be used to measure aromaticity (Weishaar et al., 2003) and molecular weight (Chowdhury, 2013) of DOM, with higher values generally indicative of higher aromaticity. $SUVA_{254}$ is calculated by dividing the absorbance at 254 nm by DOC. Detailed Chl-*a*, DOC, fluorescence DOM (FDOM), dissolved oxygen (DO), and wavelength (λ)-dependent absorption coefficients of CDOM ($a_{CDOM}(\lambda)$) were determined in the laboratory using published techniques. See supplementary information (Section S1) for analytical details.

2.7 Statistical analyses

The correlation coefficient (r) and probability (p) values were used to assess the goodness of fit. The correlation matrix, analysis of variance, and principal components analysis were performed with SPSS version 18.0 (SPSS Inc., Chicago, IL, USA) to examine potential relationships between CO, DOM parameters, and environmental factors. P values < 0.05 were considered significant. Shapiro-Wilk tests (Table S2, supplementary information) indicated that the data were normally distributed for DOC in the SSW ($p = 0.258$), but not for $[CO]_{ssw}$, $[CO]_{sml}$, $a_{CDOM}(254)$ in the SSW and SML, and DOC in the SML ($p < 0.001$ for all). Therefore, all data were analyzed consistently using non-parametric Kruskal-Wallis and Dunn-Bonferroni post-hoc tests. Pearson's

296 product-moment correlation was used to identify relationships between parameters and
297 was calculated at a 95% confidence level.

298 **3. Results**

299 *3.1 Environmental Factors and CO Concentration in the SSW and the SML*

300 Surface water temperature increased from 2.08°C at YS station H12 to 23.8°C at
301 ECS station E7 (mean value: 11.85 ± 4.53°C, Fig. 2). Surface salinity increased from
302 28.85 at Changjiang River Estuary (CRE) station E1 to 34.62 at ECS station E7 (32.35
303 ± 1.17, Fig. 2). Wind speed during sampling ranged from 0.68 m s^{-1} at station H9 to
304 12.00 m s^{-1} at station FJ1 (6.09 ± 2.50 m s^{-1}). The integrated net solar irradiance (14.09
305 ± 114.64 kW m^{-2}) during the in-situ incubation ranged from −111.8 kW m^{-2} at YS
306 station H5 to 417.9 kW m^{-2} at ECS station F4 (Table S1).

307 During the study period, $[CO]_{ssw}$ was particularly high at the station F4 (3.61 nmol
308 L^{-1}, sampling time: 12: 43) in the SML and relatively high at the station P6 (2.81 nmol
309 L^{-1}, sampling time: 14: 36) in the SSW (Fig. 2). The maximum $[CO]_{sml}$ was observed
310 during daytime, but the minimum $[CO]_{sml}$ was observed during nighttime (station E2:
311 0.59 nmol L^{-1}, sampling time: 22: 22, Fig. 3). No significant difference was observed
312 between [CO] in the SML (1.54 nmol L^{-1}) and the SSW (1.23 nmol L^{-1}) (n = 52, p =
313 0.11, Wilcoxon signed-rank test). [CO] mean value in the YS (SSW: 1.23 ± 0.40 nmol
314 L^{-1}; SML: 1.54 ± 0.68 nmol L^{-1}) was similar to the concentration observed in the ECS
315 (SSW: 1.23 ± 0.45 nmol L^{-1}; SML: 1.55 ± 0.92 nmol L^{-1}) between the SML and the
316 SSW, respectively. $a_{CDOM}(254)$ in the YS (SSW: 3.59 ± 0.89 m^{-1}; SML: 4.78 ± 0.85 m^{-}

317 ^{1}) was higher than that in the ECS (SSW: 1.64 ± 0.72 m^{-1}; SML: 4.70 ± 3.35 m^{-1}) in
318 both the SML and the SSW. $a_{CDOM}(254)$ in the SML (4.74 ± 2.50 m^{-1}) showed relatively
319 higher values compared to the SSW (2.52 ± 1.26 m^{-1}) during winter. The stronger
320 negative linear relationship observed between salinity and $a_{CDOM}(254)$ was observed in
321 the SSW ($r = -0.716$, $n = 52$, $p < 0.01$), where the influence of terrestrial input in this
322 water layer was higher than that in the SML ($r = -0.038$, $n = 52$).

323 *3.2 Variations in parallel factor analysis (PARAFAC)-derived fluorescent DOM*
324 *components and factors controlling the composition of the fluorescent components*

325 The three fluorescent DOM components were determined statistically by
326 conducting Parallel factor analysis (PARAFAC) of the samples (Table S3; Fig. S1;
327 Supplementary Information 1.2). Component C1 was apparent with excitation and
328 emission peaks at 275 nm and 335 nm, respectively, and was likely a tryptophan-like
329 peak T (Yamashita et al., 2017). C2 exhibited excitation/emission (E_x/E_m) maxima at
330 350 nm/455 nm and similar to peak C derived from terrestrial humic sources (Coble
331 and Paula, 2007). Peak C has often been observed in various coastal (Coble, 1996) and
332 oceanic environments (Yamashita et al., 2017). C3 appeared as a fluorophore with
333 E_x/E_m wavelengths of 320 nm/390 nm and was similar to marine humic-like
334 components from coastal environments (Yamashita and Jaffé, 2008).

335 *3.3 Variation and enrichment of CO, CDOM, DOC, and FDOM in the SML*

336 [CO] showed relatively higher mean value in the SML, where its EFs ranged from
337 0.34 to 3.6 and it had a mean EFs value of 1.3 ± 0.7 (Fig. 3). The absorption of CDOM
338 and the fluorescence intensity of FDOM components in the SML were positively
339 correlated with their respective SSW values (Fig. S2), indicating that transport of DOM
340 from the SSW to the SML is an important pathway. Up to 92% of CDOM samples were
341 enriched in the SML, with the average EF value of $a_{CDOM}(254)$ of 2.2 ± 1.2, ranging
342 between 0.4 and 6.7. The EFs of C3, C1 and C2 were 1.6 ± 0.7, 1.4 ± 0.6, and 1.3 ± 0.5,
343 respectively. The EFs of CO, CDOM, and DOC in the SML were generally higher in
344 the ECS than those in the YS· (Fig. 2 and Fig. S3). Furthermore, relatively higher
345 CDOM absorption slope mean values ($S_{275-295}$ and S_R) were observed in the SML (SSW:
346 $S_{275-295}$: 0.0206 ± 0.0068 and S_R: 1.48 ± 0.49; SML: $S_{275-295}$: 0.0210 ± 0.0055 and S_R:
347 1.53 ± 0.22), indicating that CDOM in the SML experienced more significant
348 photodegradation than that in the SSW. The EF of CO in the daytime (1.5 ± 0.8, 7: 00-
349 19: 00) was 1.6 times higher than that in the nighttime (0.9 ± 0.3, 19: 00-7: 00) (Fig.
350 3b)). The EF of CDOM in the daytime (2.3 ± 11.4) was 1.1 times higher than that in
351 the nighttime (2.1 ± 0.9) (Fig. 3b)). In addition, $[CO]_{ssw}$ in the daytime (1.39 ± 0.47
352 nmol L^{-1}) was 1.3 times higher than that in the nighttime (1.05 ± 0.22 nmol L^{-1}) and
353 $[CO]_{sml}$ in the daytime (1.88 ± 0.77 nmol L^{-1}) was 2.0 times higher than that in the
354 nighttime (0.95 ± 0.29 nmol L^{-1}).

3.4 Variation of sea-to-air flux of CO

The atmospheric mixing ratios ($[CO]_{atm}$) of the eastern marginal seas of China ranged from 239 to 900 ppbv, with an average of 602 ± 164 ppbv (n = 69; Fig. 2) during winter. $[CO]_{atm}$ measured at station A1 in the YS (the highest concentration) was nearly 4 times higher than that measured at station T2 in the ECS (the lowest concentration). YS showed higher CO mixing ratios (mean value: 423 ppbv in 2007; 657 ppbv in 2019) than ECS (mean value: 252 ppbv in 2007; 476 ppbv in 2019) in this study and a previous study (Yang et al., 2010), indicating that $[CO]_{atm}$ was relatively higher in the YS than the ECS. Generally, $[CO]_{atm}$ showed a significant decreasing trend from the northern to the southern regions in the eastern marginal seas of China (Fig. 2).

The instantaneous sea-to-air fluxes of CO ranged from −1.75 to 39.78 nmol m^{-2} h^{-1} in the SML (4.96 ± 7.35 nmol m^{-2} h^{-1}) and from −0.04 to 34.18 nmol m^{-2} h^{-1} in the SSW (7.40 ± 7.31 nmol m^{-2} h^{-1}). Higher fluxes mostly occurred in the southernmost part of the survey area in the ECS (Fig. 2). Although the concentrations of $[CO]_{atm}$ in the northern region (YS) were generally higher than those in the southern region (ECS), the sea-to-air fluxes of CO in the SML in the southern region (6.94 ± 9.61 nmol m^{-2} h^{-1}) were 3.5 times higher than that in the northern region (1.97 ± 2.11 nmol m^{-2} h^{-1}), indicated that the sea-to-air flux of CO did not followed $[CO]_{atm}$ shown in Fig. 2.

3.5 CO production and consumption

The photoproduction rate of CO (K_{photo}) under solar irradiance ranged from 0.71 to 1.05 nmol L^{-1} h^{-1} (0.86 ± 0.12 nmol L^{-1} h^{-1}) and 0.71 to 1.27 nmol L^{-1} h^{-1} (1.03 ± 0.16

376 nmol L^{-1} h^{-1}) during the in-situ incubation experiments in the SSW and the SML,
377 respectively, as shown in Fig. 4a) and Table S4. The mean value of K_{photo} in the SML
378 was slightly higher than that in the SSW, but the τ_{prod} was lower in the SML (1.35 h)
379 than in the SSW (1.22 h). In addition, a significant relationship was observed between
380 the light-normalized CO production rates between the SML and the SSW ($r = 0.408$, p
381 < 0.01, $n = 6$) during winter. The dark production rates of CO (k_{dark}) ranged from −0.01
382 to 4.81 nmol L^{-1} d^{-1}, with a mean value of 1.25 ± 2.34 nmol L^{-1} d^{-1} in the SSW (Table
383 S3). However, no significant dark production was observed in the SML water samples,
384 which indicated that dark production may be the main factor controlling CO
385 concentrations in deeper seawater.

386 The microbial consumption rates of CO in the SML varied greatly (0.18 ± 0.05
387 nmol L^{-1} h^{-1}), higher than the average in the SSW (0.13 ± 0.03 nmol L^{-1} h^{-1}) (Fig. 4b).
388 CO photoproduction rates were 5.7 times higher than CO consumption rates in the SML,
389 and CO photoproduction rates were 6.6 times higher than CO consumption rates in the
390 SSW. The turnover times driven by microorganism (τ_{bio}), i.e., the reciprocal of k_{bio},
391 were 8.9 ± 2.9 h and 11.9 ± 5.4 h in the SML and the SSW, respectively. τ_{bio} in the SML
392 and the SSW ranged between 1.43 and 3.78 d^{-1} (2.76 ± 0.80 d^{-1}) and between 1.17 and
393 3.48 d^{-1} (2.46 ± 0.88 d^{-1}), respectively, higher than those observed in the Arctic marginal
394 sea (0.96 ± 0.29 d^{-1}; Xie et al., 2005), but lower than those in the Northwest Atlantic
395 Ocean (6.24 ± 5.76 d^{-1}; Xie et al., 2005) and the China shelf sea (4.80 ± 1.82 d^{-1}; Zhang
396 et al., 2019). The maximum k_{bio} value appeared at the near-shore station B1 and the
397 minimum value at the offshore station S6 in the SML (Table S3). Thus, the bacterial

consumption rate constant of CO was low in oligotrophic open ocean regions but higher in productive coastal areas. Since the CO photoproduction rate in the SSW at the near-shore station B1 was lower than that of the near-shore station E2 and its CO consumption ability was much stronger, the seawater concentration of CO at coastal station E2 (1.62 nmol L^{-1}) was higher than that at coastal station B1 (1.51 nmol L^{-1}).

3.6 Primary factors controlling the distribution of the optical parameters of DOM and CO and their EFs

Negative relationships were observed between salinity and $a_{CDOM}(254)$ (SSW: $p < 0.01$, $r = -0.715$, $n = 62$; SML: $p = -0.045$, $n = 52$), $a_{CDOM}(355)$ (SSW: $p < 0.01$, $r = -0.622$; SML: $r = -0.146$), and the C1 (SSW: $p < 0.01$, $r = -0.758$; SML: $r = -0.158$), C2 (SSW: $p < 0.01$, $r = -0.341$; SML: $r = -0.106$), and C3 (SSW: $p < 0.01$, $r = -0.851$; SML: $r = -0.154$) components in SSW and SML (Table 1). High and low fluorescence levels of these three components were usually found at sites with low and high salinities, respectively (Fig. 2). These results indicated that riverine inputs mainly determined the distributions of CDOM and FDOM. $a_{CDOM}(254)$ and all three fluorescence components were also positively correlated with $SUVA_{254}$ (Table 1), indicating that CDOM showed higher aromaticity and humification in the eastern marginal seas of China. In addition, we observed a significant positive relationship between $a_{CDOM}(254)$ and Chl-*a* in the SSW ($p < 0.01$, $r = 0.333$, $n = 62$), suggesting that phytoplankton biomass and biological processes played an essential role in generating new CDOM and controlling the distribution of CDOM in winter.

Although significant CO production via CDOM photodegradation has been recorded in estuarine systems (Stubbins et al., 2011), no significant relationships were observed between [CO] and $a_{CDOM}(254)$ in either the SSW or the SML in our study regions. $a_{CDOM}(254)$ ($p < 0.01$, $r = -0.419$) and the marine humic-like C3 ($p < 0.01$, $r = -0.201$) were both negatively correlated with the flux of CO in the SML (Fig. 5a and b). The flux of CO was positively related to temperature ($p < 0.01$, $r = 0.511$) and salinity ($p < 0.01$, $r = 0.338$) in the SSW (Fig. 5), but the EF of CO showed no significant relationship with surface water temperature, salinity, or mean wind speed during sampling (Fig. 5d and 5f).

4. Discussion

4.1 CO and DOM distribution and enrichment in the SML

$[CO]_{ssw}$ showed great seasonal and diel variability, as well as variability between ocean regions. $[CO]_{ssw}$ mean value in the YS in January 2020 (1.23 ± 0.40 nmol L^{-1}) was higher than in September 2010 (1.05 nmol L^{-1}, Zhao et al., 2015). $[CO]_{ssw}$ mean value in the ECS during winter (1.23 ± 0.45 nmol L^{-1}) was also higher than in October 2021 (0.97 ± 0.86 nmol L^{-1}, Yang et al., 2024). Globally, $[CO]_{ssw}$ mean value (1.23 nmol L^{-1}) in the eastern marginal seas of China was similar to that observed in the Bohai Sea and the YS during autumn (Zhang et al., 2019, 1.22 nmol L^{-1}) and the Arctic waters of the Amundsen Gulf (Beaufort Sea) in September/October (Xie et al., 2009, 0.17–1.34 nmol L^{-1}), but was relatively lower than the Eastern Indian Ocean (Xu et al., 2023, 1.92 nmol L^{-1}). The Eastern Indian Ocean, on the other hand, had a salinity of

approximately 34 and a relatively high temperature (around 29°C) in autumn 2020 (Xu et al., 2023). Tropical and subtropical open ocean regions were generally less affected by terrestrial influences compared to estuarine, coastal and high-latitude areas. CO production and fluxes normalized to discharge are usually higher in warmer waters (Kieber et al., 2014), presumably also partly due to temperature controls on dissolution (Johnson et al., 1996). Therefore, the relatively higher concentration of $[CO]_{ssw}$ in the open ocean (ECS) might be characterized by the relatively high seawater temperature and/or strong production processes during our sampling period.

The results showed that no significant enrichment of CO in SML during the investigation, and CO enrichment in SML only occurred at 25 stations. Earlier studies have shown that the diurnal variation of $[CO]_{ssw}$ in sea surface concentration, which was first noted in the Atlantic Ocean by Swinnerton et al. (1970) with a characteristic minimum just before dawn and a maximum in the early afternoon. This cycle was subsequently observed in other expeditions in both the Pacific and Atlantic Oceans (Matsueda et al., 2000; Rhee, 2000; Ren et al., 2010; Yang et al., 2010; Yang et al., 2011). Here, $[CO]_{ssw}$, $[CO]_{sml}$ and the EFs of CO also showed strong diurnal fluctuations (Fig. 3, Section 3.1 and 3.3). Significant positive relationships were observed between the EFs of CO and the net solar irradiance (Table 2), likely resulting from the sunlight-induced photochemical production of CO during daytime and the stronger microbial consumption at night. The higher EF values of CO also occurred in the daytime, suggesting that sufficient light and higher temperatures combined to facilitate the photoproduction of CO and its enrichment in the SML.

CO, CDOM, and FDOM were more frequently enriched in the ECS (Fig. 2). DOC and CDOM decreased from coastal regions to the open ocean, and decreased from the northern sampling area (the YS) to the southern sampling area (the ECS) in both the SSW and the SML (Fig. 2), which was likely due to the input from the land-based sources (Yang et al., 2022). Moreover, atmospheric deposition of organic carbon and nutrients was found to peak in winter over the coastal ECS (Wang et al., 2019). Although the source of CDOM originated from allochthonous terrestrial sources in the ECS and the YS (Yang et al., 2021), the sink of CDOM in the ECS was more dominated by photochemical degradation processes (Zhu et al., 2018). The EF of marine humic-like Component 3 was significantly higher than the other fluorescence components (1.6 vs. 1.4 and 1.3), indicating that in-situ autochthonous DOM was more strongly enriched in the SML than terrestrial DOM. Thus, CO, CDOM, and FDOM were more frequently enriched in the open ocean (ECS), which was attributed mainly to the significant local photoproduction. Further, one note of the study of gases in the SML is that gases supersaturated with respect to their atmospheric concentrations, including CO, are inevitably lost from SML samples during sampling, depending on environmental conditions such as water temperature and wind. For example, in case of dimethylsulfide (DMS), a volatile gas with large concentration difference between the atmosphere and the ocean, Yang et al. (2001 and 2005) showed about 50–70% and 60% (mean) of loss from SML samples collected using a mesh screen at 0–15°C and at a water temperature of 10°C and wind speed of 4 m s^{-1}, respectively. A mesh screen was also used in this study, and parameters such as $[CO]_{sml}$ and the EF of CO may have been underestimated.

4.2 Photochemical and dark CO production and biological CO consumption in the SML and the SSW

Photochemical CO production is the most active in the SML, the mean photoproduction rate of CO in the SML was 1.1 times higher than that in the SSW in the eastern marginal seas of China. CO in our study region showed a longer turnover time than the findings of Sugai et al. (2021) in Sagami Bay, Japan (τ_{prod} = 0.09 h), which is probably due to the relatively low photochemical CO production rate in the SML and/or the higher photochemical degradability of CDOM in the SML under more intense light conditions in our study region.

The turnover times driven by sea-to-air exchange were much longer than those of microbial consumption, about 219 h and 1029 h in the SSW and SML, respectively. This indicated that microbial removal of CO was much faster than sea-to-air exchange, which may make the latter a subordinate pathway for CO removal in our study regions. Relatively higher microbial consumption rate of CO in marine systems has been historically attributed to higher Chl-*a*, but lower salinity level (Xie et al., 2009; Yang et al., 2010; Xu et al., 2023). In addition, the heterotrophic bacterial abundance in the SML was ~ 7.5 times greater than in the SSW and the ECS in March 2017 (Sun et al., 2020). The SML is an aggregate-enriched biofilm environment with distinct microbial communities, the diversity of which can differ significantly from underlying waters (Liss and Duce, 2005; Cunliffe et al., 2013). This higher abundance of bacteria could result in the rapid consumption of CO, along with a wide variety of other organic substances in the SML. Moreover, elevated nutrient concentrations can stimulate the

506 growth of phytoplankton, biological activity, and subsequently lead to abundant
507 primary production in the SML (Yang et al., 2022). Therefore, compared to the SSW,
508 the elevated DOM concentrations and bacteria abundances could enhance the
509 influences of photoproduction and microbial consumption on CO cycling processes in
510 the SML.

511 *4.3 Implications of CO sea-to-air exchange and emission to the atmosphere*

512 Based on the areas of the ECS (7.7×10^5 km^2) and YS (3.8×10^5 km^2) and their
513 respective CO sea-to-air fluxes, the releases of CO from the ECS and YS to the
514 atmosphere were estimated to range from 3 to 230 Mg CO-C month^{-1} (Mg = 10^6 g) and
515 from –0.2 to 880 Mg CO-C month^{-1}, with averages of 70 Mg CO-C month^{-1} and 10 Mg
516 CO-C month^{-1}, respectively. Clearly, the average annual release of CO to the
517 atmosphere in the ECS was much higher (nearly 7 times) than in the YS. Yang et al.
518 (2010) suggested that $[CO]_{ssw}$ was the main factor affecting the sea-to-air flux of CO,
519 but $[CO]_{ssw}$ in the ECS was similar to that in the YS. The lower temperatures and
520 especially reduced wind speeds may hinder its outgassing to the atmosphere. The higher
521 $[CO]_{atm}$ at the northern stations (the YS) was representative of the regionally polluted
522 continental outflow air mass due to the anthropogenic activity in East Asia. Therefore,
523 $[CO]_{atm}$ values in the YS were heavily dependent on land anthropogenic input, but in
524 the ECS, the distribution of $[CO]_{atm}$ was more dependent on the sea-to-air flux of CO.
525 As noted above, the most probable sources of CO in the SML of these sea regions
526 are in-situ photoproduction from DOM and/or vertical export through underlying SSW

water. Actually, surface-active surfactants are ubiquitous and accumulate in the uppermost < 1000 μm in seawater (Rickard et al., 2019), where they slow the rate of gas exchange between seawater and air (Cunliffe et al., 2013). Rickard et al. (2022) observed that the first-order estimates of the potential suppression of the gas transfer velocity (*kw*) by photo-derived surfactants were 12.9%–22.2% in coastal North Sea water. The highest SML enrichments in surfactants have been seen in low productivity, oligotrophic regions away from terrestrial influences, where surfactant concentrations in SSW are generally low (Wurl et al., 2016). Pereira et al. (2018) also noted that the observed reduction in the air-to-sea CO_2 exchange in the Atlantic Ocean was due to biological surfactants acting as physical barriers and altering turbulent transfer near the water surface. Therefore, the relatively lower fluxes of CO observed in the YS may indicate that seawater contains lots of DOM (surfactants) in the SML. Despite the clear importance of surfactants at the sea-to-air interface, we did not conduct surfactant-specific analyses due to the analytical limitations. In our experiments, the CO flux varied by 131% in winter. The negative correlations between $a_{CDOM}(254)$ and the sea-to-air flux of CO, and between marine humic-like C3 and the sea-to-air flux of CO, suggested that CDOM concentration may reduce the CO sea-to-air gas exchange rate in our study regions (Fig. 5a and 5b). In addition, low wind speeds may lead to high DOM enrichment, but in the meantime give rise to low sea-to-air fluxes as well. Therefore, due to the complexity of the DOM pool in the SML and its may result in decreased sea-to-air flux of CO, more measurements are needed to validate our

548 conceptual model and provide a better understanding of the flux measurements of CO
549 in the SML.

550 *4.4 Modeling of CO dynamics in the SML and the SSW*

551 All sources and sinks, including photoproduction and dark production, microbial
552 consumption and sea-to-air emission, should be considered in estimating CO dynamics
553 in the SML and SSW (Fig. 6). The effective solar illumination period of each day was
554 approximately 12 h, and based on this the average photoproduction rates in the SML
555 and the SSW were calculated to be 12.41 ± 1.87 nmol L^{-1} d^{-1}, 10.32 ± 1.48 nmol L^{-1} d^{-}
556 ^{1}, respectively. In the SSW, the ratio of photoproduction to dark production (1.88 ± 2.89
557 nmol L^{-1} d^{-1}) was about 4:1, and dark production accounted for about 15% of the total
558 production. No dark production of CO was observed in the SML. CO photoproduction
559 was lower in deeper water, while dark production was higher. The calculated
560 contribution of dark production to CO production in this study was similar to that for
561 the St. Lawrence estuary (14%; Zhang and Xie, 2012) but much lower than for the
562 Eastern Indian Ocean (20%; Xu et al., 2023). These were because dark production
563 needs to be given more weight in estimating its contribution to the total production of
564 CO in the deeper waters of the ocean than in estuaries (Xu et al., 2023). The total
565 removal rates of CO were about 2.64 nmol L^{-1} d^{-1} and 2.88 nmol L^{-1} d^{-1} in the SSW and
566 the SML, respectively, including the microbial consumption rates of 2.46 ± 0.88 nmol
567 L^{-1} d^{-1} and 2.76 ± 0.80 nmol L^{-1} d^{-1} in the SSW and the SML, respectively. The sea-to-
568 air exchange rates were 0.18 ± 0.18 nmol L^{-1} d^{-1} in the SSW and 0.12 ± 0.18 nmol L^{-1}

569 d^{-1} in the SML. The turnover of CO occurred faster in the SML environment than in the
570 SSW (~ 1.2 times). Microbial consumption was the primary sink of CO, accounting for
571 about 95% of CO removal, indicating that the biogeochemical cycling of CO is almost
572 entirely contained within seawater and only a small amount of CO is released into the
573 atmosphere (Xie et al., 2005; Yang et al., 2010; Zhang et al., 2019; Xu et al., 2023).
574 The production rates of CO in both SML and SSW significantly exceed the loss rates,
575 this could lead to the accumulation of CO in these systems. Therefore, CO balance in
576 the ECS and YS indicated that the underlying loss of CO (via sea-to-air flux and
577 biodegradation) was slower than the production of CO in the SML, therefore, a positive
578 CO balance was maintained in the SML.

579 The average annual photoproduction, microbial consumption, and sea-to-air flux
580 of CO in the SSW were about 3.02, 1.58, and 0.04 Gg CO-C $month^{-1}$, respectively,
581 based on the area of the survey region (~ 1.2×10^6 km^2, SSW ~ 10 m). Conte et al.
582 (2019) used the NEMO-PISCES model combined with original ocean CO data
583 collected worldwide over the last 50 years, ultimately estimating that global emissions
584 of CO to the atmosphere were 4.0 Tg CO-C yr^{-1} (Tg = 10^{12} g). Based on our data, we
585 estimated the contribution of China's eastern marginal seas to global marine CO
586 emissions via sea-to-air flux to be ~ 0.3‰, and the YS and the ECS occupy 2.7‰ of
587 the global ocean area. The simulated surface CO concentrations and sea-to-air fluxes
588 based on our measured values were much smaller than those simulated by Erickson
589 (1989). In our study, CO produced can be rapidly consumed by microorganisms and
590 only a small fraction was released into the atmosphere, which may explain why the

591 relative contribution of the eastern marginal seas of China to atmospheric CO was much
592 lower than the global level.

593 Notably, the enrichment of CO in the SML was more common during the daytime
594 when photochemical processes were more active, but natural sunlight can inhibit the
595 microbial consumption of CO. CO was maximal in the SML, leading to the significant
596 enrichment and supersaturation. CDOM in the SML experienced more significant
597 photodegradation than that in the SSW, as can be seen in Section 3.3. Moreover,
598 researchers assumed that biological, chemical and physical processes in the SML are
599 controlled by changes in DOM concentration at this uppermost thin boundary layer
600 between the ocean and the atmosphere (Cunliffe et al., 2013). We found that
601 autochthonous humic-like DOM was more enriched in the SML than terrestrial DOM,
602 indicating that it could be an indispensable part of CO photoproduction (Yang et al.,
603 2022). Solar irradiance was positively related to the EFs of CO (Table 2), suggesting
604 that the integrated solar irradiance influenced CO enrichment in the SML. Moreover,
605 we did discover the potential for CDOM accumulation in the SML to prevent CO
606 emissions into the atmosphere (Section 4.3). Therefore, CDOM accumulation and the
607 production rates of CO in the SML significantly exceed the loss rates, which could lead
608 to the significant accumulation of CO in the SML, especially in the daytime.

609 **5. Conclusions**

610 This study is the first comprehensive analysis of CO distribution, loss, and
611 production in both the SML and SSW, as well as sea-to-air CO flux in the ECS and YS
612 during winter. $[CO]_{ssw}$, $[CO]_{sml}$, CDOM, FDOM, and DOC generally decreased from

coastal regions toward the open ocean. However, the EFs of CO, CDOM, FDOM, and DOC were significantly higher in offshore areas, indicating that stronger enrichment and/or production processes in the SML are more common in open waters than nearshore. CDOM absorption slope mean values ($S_{275-295}$ and S_R) showed that CDOM in the SML experienced more extensive photodegradation than in the SSW. Notably, the EF of the marine humic-like component C3 was significantly higher than other fluorescence components, suggesting that in-situ autochthonous DOM was more strongly enriched in the SML compared to terrestrial DOM. Significant negative correlations were observed between $a_{CDOM}(254)$ and sea-to-air CO flux, as well as between sea-to-air CO flux and humic-like C3 in the SML, indicating that the open sea had lower CDOM concentrations but greater suppression of CO gas transfer compared to nearshore waters. This suggests that DOM enrichment may influence CO emissions to the atmosphere in the SML. The diurnal variability in CO EF and $[CO]_{sml}$ indicates that in-situ photoproduction processes are vital in shaping CO distribution within the SML. Our results demonstrate a complex interaction between DOM enrichment and sea-to-air CO fluxes in the SML, which should be incorporated into future carbon budget models for more accurate assessments of carbon cycling in marine environments.

Author contribution

Lin Yang: Conceptualization, Writing-Original Draft, Writing-Review and Editing

Bin Yang: Writing-Review and Editing

Jing Zhang: Writing-Review and Editing, Funding acquisition

Anja Engel: Writing-Review and Editing

Gui-Peng Yang: Writing-Review and Editing, Supervision

Competing interests

The authors declare that they have no known competing financial interests or personal relationships that could have appeared to influence the work reported in this paper.

Acknowledgment

We are grateful to the captain and crew of the R/V "*Dong Fang Hong 3*" for their help and cooperation during the in-situ investigation. This study was financially supported by the National Natural Science Foundation of China (Grant No. 42330402), and the National Key Research and Development Program (Grant No. 2016YFA0601300).

References

Chen, C.T.A., 2009. Chemical and physical fronts in the Bohai, Yellow and East China seas. J. Mar. Syst. 78(3), 394–410. doi: 10.1016/j.jmarsys.2008.11.016

Chen, Y., Yang, G., Xia, Q., Wu, G., 2016. Enrichment and characterization of dissolved organic matter in the surface microlayer and subsurface water of the South Yellow Sea. Mar. Chem. 182(Mar. 20), 1–13. doi: 10.1016/j.marchem.2016.04.001

Chowdhury, S., 2013. Trihalomethanes in drinking water: effect of natural organic matter distribution. WATER SA, 39, 1–7. doi: 10.4314/wsa.v39i1.1

Coble, P.G., 1996. Characterization of marine and terrestrial DOM in seawater using excitation-emission matrix spectroscopy. 51(4), 325–346. doi: 10.1016/0304-4203(95)00062-3

Coble, P.G., Paula, G., 2007. Marine optical biogeochemistry: the chemistry of ocean color. Cheminform 38(2), 402–418. doi: 10.1002/chin.200720265

Conte, L., Szopa, S., Séférian, R., Bopp, L., 2019. The oceanic cycle of carbon monoxide and its emissions to the atmosphere. Biogeosciences, 16(4), 881–902. doi: 10.5194/bg-16-881-2019

Cordero, P.R.F., Bayly, K., Leung, P.M., Huang, C., Greening, C., 2019. Atmospheric carbon monoxide oxidation is a widespread mechanism supporting microbial survival. ISME J. 13(14). doi: 10.1038/s41396-019-0479-8

Cory, R.M., Kling, G.W., 2018. Interactions between sunlight and microorganisms influence dissolved organic matter degradation along the aquatic continuum. Limnol. Oceanogr. Lett. 3(3), 102–116. doi: 10.1002/lol2.10060

669 Cunliffe, M., Engel, A., Frka, S., Gašparovi, B., Guitart, C., Murrell, J.C., Salter, M.,
670 Stolle, C., Upstill-Goddard, R., Wurl, O., 2013. Sea surface microlayers: A unified
671 physicochemical and biological perspective of the air-ocean interface. Prog.
672 Oceanogr. 109, 104–116. doi: 10.1016/j.pocean.2012.08.004

673 Cunliffe, M., Upstill-Goddard, R.C., Murrell, J.C., 2011. Microbiology of aquatic
674 surface microlayers. FEMS Microbiol. Rev. 35(2), 233–246. doi:
675 10.1111/j.1574‐6976.2010.00246.x

676 Cunliffe, M., Wurl, O., 2014. Guide to best practices to study the ocean's surface.
677 Occasional Publications of the Marine Biological Association of the United
678 Kingdom, Plymouth, UK. 118 pp.

679 Doney, S.C., Najjar, R.G., Stewart, S., 1995. Photochemistry, mixing and diurnal cycles
680 in the upper ocean. J. Mar. Res. 53(3), 341–369. doi: 10.1357/0022240953213133

681 Edson, J.B., Fairall, C.W., Bariteau, L., Zappa, C.J., Cifuentes-Lorenzen, A., Mcgillis,
682 W.R., Pezoa, S., Hare, J.E., Helmig, D., 2011. Direct covariance measurement of
683 CO_2 gas transfer velocity during the 2008 Southern Ocean Gas Exchange
684 Experiment: Wind speed dependency. J. Geophys. Res. 116(C4), 1943–1943. doi:
685 10.1029/2011jc007022

686 Engel, A., Galgani, L., 2016. The organic sea-surface microlayer in the upwelling
687 region off the coast of Peru and potential implications for air–sea exchange
688 processes. Biogeosciences 13, 989–1007. doi: 10.5194/bg-13-989-2016

689 Erickson, D.J., 1989. Ocean to atmosphere carbon monoxide flux: Global inventory
690 and climate implications. Global Biogeochem. Cyc. 3(4), 305–314. doi:
691 10.1029/GB003i004p00305

692 Fichot, C.G., Miller, W.L., 2010. An approach to quantify depth-resolved marine
693 photochemical fluxes using remote sensing: application to carbon monoxide (CO)
694 photoproduction. Remote Sens. Environ. 114, 1363–1377. doi:
695 10.1016/j.rse.2010.01.019

696 Garrett, W.D., 1965. Collection of slick-forming materials from the sea surface. Limnol.
697 Oceanogr. 10(1965), 602–605. doi: 10.2307/2833459

698 Gros, V., Peeken, I., Bluhm, K., Zöllner, E., Sarda-Esteve, R., Bonsang, B., 2009.
699 Carbon monoxide emissions by phytoplankton: evidence from laboratory
700 experiments. Environ. Chem. 6, 369–379. doi: 10.1071/EN09020

701 Guallar, C., Flos, J., 2019. Linking phytoplankton primary production and
702 chromophoric dissolved organic matter in the sea. Prog. Oceanogr. 176, 102116.
703 doi: 10.1016/j.pocean.2019.05.008

704 Huang, Y.J., Brimblecombe, P., Lee, C.L., Latif, M.T., 2015. Surfactants in the sea-
705 surface microlayer and sub-surface water at estuarine locations: Their
706 concentration, distribution, enrichment, and relation to physicochemical
707 characteristics. Mar. Pollut. Bull. 97(1–2), 78–84. doi:
708 10.1016/j.marpolbul.2015.06.031

709 Jones, R.D., Amador, J.A., 1993. Methane and carbon monoxide production, oxidation,
710 and turnover times in the Caribbean Sea as influenced by the Orinoco River. J.
711 Geophys. Res. 98(C2), 2353–2359. doi: 10.1029/92JC02769

712 Johnson, J.E., Bates, T.S., 1996. Sources and sinks of carbon monoxide in the mixed
713 layer of the tropical south Pacific Ocean. Global Biogeochem. Cy. 10(2), 347–359.
714 doi: 10.1029/96GB00366

715 Kettle, A.J., 2005. Diurnal cycling of carbon monoxide (CO) in the upper ocean near
716 Bermuda. Ocean Model. 8(4), 337–367. doi: 10.1016/j.ocemod.2004.01.003
717 Kieber, D.J., Miller, G.W., Neale, P.J., Mopper, K., 2014. Wavelength and temperature-
718 dependent apparent quantum yields for photochemical formation of hydrogen
719 peroxide in seawater. Env. Sci.: Processes Impacts. doi: 10.1039/C4EM00036F.
720 Li, Y., He, Z., Yang, G.P., Wang, H., Zhuang, G.C., 2019. Volatile halocarbons in the
721 marine atmosphere and surface seawater: diurnal and spatial variations and
722 influences of environmental factors. Atmos. Environ. 214, 116820.
723 10.1016/j.atmosenv.2019.116820
724 Li, Y., Fichot, C.G., Geng, L., Scarratt, M.G., Xie, H., 2020. The Contribution of
725 Methane Photoproduction to the Oceanic Methane Paradox. Geophys. Res. Lett.
726 47(14), 1–10. doi: 10.1029/2020GL088362
727 Liss, P.S., Merlivat, L., 1986. Air-sea gas exchange rates: Introduction and synthesis.
728 In P. Buat-Ménard (Ed.), The role of air-sea exchange in geochemical cycling, (pp.
729 113–127). Dordrecht, Netherlands: Springer. Retrieved from
730 papers3://publication/uuid/BAFDE7E6-A29C-466C-B1CD-2A7DAFF930D5
731 Liss, P.S., Duce, R.A., (Eds) 1997. The sea surface and global change. Cambridge, UK:
732 Cambridge University Press.
733 Liss, P.S., Duce, R.A., 2005. The Sea Surface and Global Change, Cambridge
734 University Press, UK, ISBN-13: 978-0511525025.
735 Lønborg, C., Álvarez-Salgado, X.A., Duggan, S., Carreira, C., 2018. Organic matter
736 bioavailability in tropical coastal waters: The Great Barrier Reef. Limnol.
737 Oceanogr. 63, 1015–1035. doi: 10.1002/lno.10717

738 Ma, Q.Y., Yang, G.P., 2023. Roles of phytoplankton, microzooplankton, and bacteria
739 in DMSP and DMS transformation processes in the East China Continental Sea.
740 Prog. Oceanogr. 103003. doi: 10.1016/j.pocean.2023.103003
741 Mopper, K., Kieber, D.J., 2002. Photochemistry and cycling of carbon, sulfur, nitrogen
742 and phosphorus. In: Hansell, D.A., Carlson, C.A. (Eds.), Biogeochemistry of
743 Marine Dissolved Organic Matter. AP. doi: 10.1016/b978-012323841-2/50011-7
744 Nelson, E.D., McConnell, L.L., Baker, J.E., 1998. Diffusive Exchange of Gaseous
745 Polycyclic Aromatic Hydrocarbons and Polychlorinated Biphenyls Across the
746 Air−Water Interface of the Chesapeake Bay. Environ. Sci. Technol. 32(7), 912–
747 919. doi: 10.1021/es9706155
748 Nguyen, N.H., Turner, A.J., Yin, Y., Prather, M.J., Frankenberg, C., 2020. Effects of
749 chemical feedbacks on decadal methane emissions estimates. Geophys. Res. Lett.
750 47(3), e2019GL085706. doi: 10.1029/2019GL085706
751 Obernosterer, I., Catala, P., Reinthaler, T., Herndl, G.J., Lebaron, P., 2006. Enhanced
752 heterotrophic activity in the surface microlayer of the Mediterranean Sea. Aquat.
753 Microb. Ecol. 39, 293–302. doi: 10.3354/ame039293
754 Obernosterer, I., Catala, P., Lami, R., Caparros, J., Ras, J., Bricaud, A., Dupuy, C., van
755 Wambeke, F., Lebaron, P., 2008. Biochemical characteristics and bacterial
756 community structure of the sea surface microlayer in the South Pacific Ocean.
757 Biogeosciences, 5, 693–705. doi: 10.5194/bg-5-693-2008

758 Orellana, M.V., Matrai, P.A., Leck, C., Rauschenberg, C.D., Lee, A.M., Coz, E., 2011.
759 Marine microgels as a source of cloud condensation nuclei in the high Arctic. Proc.
760 Natl. Acad. Sci. 108, 13612–13617. doi: 10.1073/pnas.1102457108.
761 Pereira, R., Schneider-Zapp, K., Upstill-Goddard, R.C., 2016. Surfactant control of gas
762 transfer velocity along an offshore coastal transect: results from a laboratory gas
763 exchange tank. Biogeosciences, 13, 3981–3989. doi: 10.5194/bg-13-3981-2016.
764 Pereira, R., Ashton, I., Sabbaghzadeh, B., Shutler, J.D., Upstill-Goddard, R.C., 2018.
765 Reduced air–sea CO_2 exchange in the Atlantic Ocean due to biological surfactants.
766 Nat. Geosci. 11, 492–496. doi: 10.1038/s41561-018-0136-2
767 Ren, C., Yang, G., Lu, X., 2014. Autumn photoproduction of carbon monoxide in
768 Jiaozhou Bay China. J. Ocean U. China, 13(3), 428–436. doi: 10.1007/s11802-
769 014-2225-1
770 Rickard, P.C., Uher, G., Upstill-Goddard, R.C., Frka, S., Mustaffa, N.I.H., Banko-Kubis,
771 H.M., Hanne Marie, B.K., Ana Cvitesic, K., Blazenka, G., Christian, S., Oliver,
772 W., Ribas-Ribas, M., 2019. Reconsideration of seawater surfactant activity
773 analysis based on an inter-laboratory comparison study. Mar. Chem. 208, 103–111.
774 doi: 10.1016/j.marchem.2018.11.012
775 Rickard, P.C., Uher, G., Upstill Goddard, R.C., 2022. Photo reactivity of surfactants in
776 the sea surface microlayer and subsurface water of the Tyne estuary, UK. Geophys.
777 Res. Lett. 49(4), e2021GL095469. doi: 10.1029/2021GL095469
778 Sabbaghzadeh, B., Upstill-Goddard, R.C., Beale, R., Pereira, R., Nightingale, P.D.,
779 2017. The Atlantic Ocean surface microlayer from 50°N to 50°S is ubiquitously
780 enriched in surfactants at wind speeds up to 13 m s^{-1}. Geophys. Res. Lett. 44(6),
781 2852–2858. doi: 10.1002/2017GL072988

782 Shaharom, S., Latif, M.T., Khan, M.F., Yusof, S.N.M., Sulong, N.A., Wahid, N.B.A.,
783 Uning, R., Suratman, S., 2018. Surfactants in the sea surface microlayer,
784 subsurface water and fine marine aerosols in different background coastal areas.
785 Environ. Sci. Pollut. Res. Int. 25(27), 27074–27089. doi: 10.1007/s11356-018-
786 2745-0
787 Song, G., Richardson, J.D., Werner, J.P., Xie, H., Kieber, D.J., 2015. Carbon monoxide
788 photoproduction from particles and solutes in the Delaware estuary under
789 contrasting hydrological conditions. Environ. Sci. Technol. 49(24), 14048–14056.
790 doi: 10.1021/acs.est.5b02630
791 Stedmon, C.A., Markager, S., Bro, R., 2003. Tracing dissolved organic matter in
792 aquatic environments using a new approach to fluorescence spectroscopy. Mar.
793 Chem. 82(3–4), 239–254. doi: 10.1016/S0304-4203(03)00072-0
794 Stubbins, A., Uher, G., Kitidis, V., Law, C.S., Upstill-Goddard, R.C., Woodward,
795 E.M.S., 2006. The open-ocean source of atmospheric carbon monoxide. Deep-Sea
796 Res. Part II, 53, 1685–1694. doi: 10.1016/j.dsr2.2006.05.010
797 Stubbins, A., Law, C., Uher, G., Upstill-Goddard, R., 2011. Carbon monoxide apparent
798 quantum yields and photoproduction in the Tyne estuary. Biogeosciences 8, 703–
799 713. doi:10.5194/bg-8-703-2011
800 Sugai, Y., Tsuchiya, K., Shimode, S., Toda, T., 2021. Photochemical Production and
801 Biological Consumption of CO in the SML of Temperate Coastal Waters and Their
802 Implications for Air-Sea CO Exchange. J. Geophys. Res.: Oceans 125(4), 1–14.
803 doi: 10.1029/2019JC015505
804 Sun, H., Zhang, Y.H., Tan, S., Zheng, Y.F., Zhou, S., Ma, Q.Y., Yang, G.P., Todd, J.,
805 Zhang, X.H., 2020. DMSP-Producing Bacteria Are More Abundant in the Surface

Microlayer than Subsurface Seawater of the East China Sea. Microb. Ecol. 80, 350–365. doi: 10.1007/s00248-020-01507-8

Troxler, R.F., 1972. Synthesis of bile pigments in plants. Formation of carbon monoxide and phycocyanobilin in wild-type and mutant strains of the alga, Cyanidium caldarium. Biochemistry 11(23), 4235–4242. doi: 10.1021/bi00773a007

Tsai, W.T., Liu, K.K., 2003. An assessment of the effect of sea surface surfactant on global atmosphere–ocean CO_2 flux. J. Geophys. Res.: Oceans 108, 3127. doi: 10.1029/2000jc000740

Wang, H., Sun, F., Liu, W., 2020. Characteristics of Streamflow in the Main stream of Changjiang River and the Impact of the Three Gorges Dam. Catena 104498. doi: 10.1016/j.catena.2020.104498

Weishaar, J.L., Aiken, G.R., Bergamaschi, B.A., Fram, M.S., Fujii, R., Mopper, K., 2003. Evaluation of specific ultraviolet absorbance as an indicator of the chemical composition and reactivity of dissolved organic carbon. Environ. Sci. Technol. 37, 4702–4708. doi: 10.1021/es030360x

Wiesenburg, D.A, Guinasso, N.L., 1979. Equilibrium solubilities of methane, carbon monoxide, and hydrogen in water and sea water. J. Chem. Eng. Data, 24(4), 356–360. doi: 10.1021/je60083a006

Wurl, O., Miller, L., Röttgers, R., Vagle, S., 2009. The distribution and fate of surface-active substances in the sea-surface microlayer and water column. Mar. Chem. 115, 1–9. doi: 10.1016/j.marchem.2009.04.007

Wurl, O., Stolle, C., Thuoc, C.V., Thu, P.T., Mari, X., 2016. Biofilm-like properties of the sea surface and predicted effects on air-sea CO_2 exchange. Prog. Oceanogr. 144, 15–24. doi: 10.1016/j.pocean.2016.03.002

Xie, H., Andrews, S.S., Martin, W.R., Miller, J., Zafiriou, O.C., 2002. Validated methods for sampling and headspace analysis of carbon monoxide in seawater. Mar. Chem. 77(2), 93–108. doi: 10.1016/S0304-4203(01)00065-2

Xie, H., Zafiriou, O.C., Umile, T.P., Kieber, D.J., 2005. Biological consumption of carbon monoxide in Delaware Bay, NW Atlantic and Beaufort Sea. Mar. Ecol. Prog. Seri. 290, 1–14. doi: 10.3354/meps290001

Xie, H.X., Bélanger, S., 2009. Photobiogeochemical cycling of carbon monoxide in the southeastern Beaufort Sea in spring and autumn. Limnol. Oceanogr. 54(1), 234–249. doi: 10.4319/lo.2009.54.1.0234

Xu, G.B., Xu, F., Ji, X., Zhang, J., Yan., S.B., Mao, S.H., Yang, G.P., 2023. Carbon monoxide cycling in the Eastern Indian Ocean. J. Geophys. Res. Oceans 128(5). doi: 10.1029/2022JC019411

Yamashita, Y., Hashihama, F., Saito, H., Fukuda, H., Ogawa, H., 2017. Factors controlling the geographical distribution of fluorescent dissolved organic matter in the surface waters of the Pacific Ocean. Limnol. Oceanogr. 62(6), 2360–2374. doi: 10.1002/lno.10570

Yamashita, Y., Jaffé, R., 2008. Characterizing the interactions between trace metals and dissolved organic matter using excitation-emission matrix and parallel factor analysis. Environ. Sci. Technol. 42(19), 7374–7379. doi: 10.1021/es801357h

Yang, G.P., Watanabe, S., Tsunogai, S., 2001. Distribution and cycling of dimethylsulfide in surface microlayer and subsurface seawater. Mar. Chem. 76(3), 137–153. doi: 10.1016/S0304-4203(01)00054-8

Yang, G.P., Ren, C.Y., Lu, X.L., Liu, C.Y., Ding, H.B., 2011. Distribution, flux, and photoproduction of carbon monoxide in the East China Sea and Yellow Sea in spring. J. Geophys. Res.: Oceans 116(C2), C02001. doi: 10.1029/2010jc006300

Yang, G.P., Wang, W.L., Lu, X.L., Ren, C.Y., 2010. Distribution, flux and biological consumption of carbon monoxide in the Southern Yellow Sea and the East China Sea. Mar. Chem. 122(1–4), 74–82. doi: 10.1016/j.marchem.2010.08.001

Yang, G.P., Tsunogai, S., Watanabe, S., 2005. Biogeochemistry of Dimethylsulfoniopropionate (DMSP) in the Surface Microlayer and Subsurface Seawater of Funka Bay, Japan. J. Oceanogr. 61, 69–78. doi: 10.1007/s10872-005-0020-8

Yang, L., Zhang, J., Yang, G.P., 2021. Mixing behavior, biological and photolytic degradation of dissolved organic matter in the East China Sea and the Yellow Sea. Sci. Total Environ. 762(6), 143164. doi: 10.1016/j.scitotenv.2020.143164

Yang, L., Zhang, J., Engel A., Yang, G.P., 2022. Spatio-temporal distribution, photoreactivity and environmental control of dissolved organic matter in the sea-surface microlayer of the eastern marginal seas of China. Biogeosciences, 19, 5251–5268. doi: 10.5194/bg-19-5251-2022

Yang, L., Gong, C.Y., Mo, X.J., Zhang, J., Yang, B., Yang, G.P., 2024. Carbon monoxide in the marine atmosphere and seawater: Spatiotemporal distribution and photobiogeochemical cycling. J. Geophys. Res.: Oceans, 129(8), e2024JC021286. doi: 10.1029/2024JC021286

874 Yu, C., Lu, C., Li, Y., Li, H., Lin, J., Chang, L., 2025. Spatial and temporal variation
875 of nutrient distribution in the Yangtze River estuary and adjacent waters: insights
876 from GOCI data analysis. Mar. Environ. Res. 204. doi:
877 10.1016/j.marenvres.2024.106895
878 Zafiriou, O.C., Andrews, S.S., Wang W., 2003. Concordant estimates of oceanic carbon
879 monoxide source and sink processes in the Pacific yield a balanced global "blue-
880 water" CO budget. Global Biogeochem. Cy. 17(1), 1015–1027. doi:
881 10.1029/2001gb001638
882 Zafiriou, O.C., Xie, H., Nelson, N.B., Wang, N.W., 2008. Diel carbon monoxide
883 cycling in the upper Sargasso Sea near Bermuda at the onset of spring and in
884 midsummer. Limnol. Oceanogr. 53(2), 835–850. doi: 10.2307/40006463
885 Zhang, J., Liu, S.M., Ren, J.L., Wu, Y., Zhang, G.L., 2007. Nutrient gradients from the
886 eutrophic Changjiang (yangtze river) estuary to the oligotrophic kuroshio waters
887 and re-evaluation of budgets for the east China sea shelf. Prog. Oceanog. 74(4),
888 449–478.
889 Zhang, J., Wang, J., Zhuang, G.C., Yang G.P., 2019. Carbon monoxide cycle in the
890 Bohai Sea and the Yellow Sea: Spatial variability, sea-air exchange and biological
891 consumption in autumn. J. Geophys. Res.: Oceans 124, 4248–4257. doi:
892 10.1029/2018JC014864
893 Zhang, Y., Xie, H., 2012. The sources and sinks of carbon monoxide in the St.
894 Lawrence system. Deep-Sea Res. Part II: Topical Studies in Oceanography 81,
895 114–123. doi: 10.1016/j.dsr2.2011.09.003
896 Zhang, Y., Xie, H., Chen, G., 2006. Factors affecting the efficiency of carbon monoxide
897 photoproduction in the St. Lawrence estuarine system (Canada). Environ. Sci.
898 Technol. 40(24), 7771–7777. doi: 10.1021/es0615268

899 Zhang, Y., Xie, H., Fichot, C.G., Chen, G., 2008. Dark production of carbon monoxide
900 (CO) from dissolved organic matter in the St. Lawrence estuarine system:
901 Implication for the global coastal and blue water CO budgets. J. Geophys. Res.:
902 Oceans 113(12), 1–9. doi: 10.1029/2008JC004811
903 Zhu, W.Z., Zhang, H.H., Zhang, J., Yang, G.P., 2018. Seasonal variation in
904 chromophoric dissolved organic matter and relationships among fluorescent
905 components, absorption coefficients, and dissolved organic carbon in the Bohai
906 Sea, the Yellow Sea and the East China Sea. J. Mar. Syst. 180, 9–23. doi:
907 10.1016/j.jmarsys.2017.12.003
908

Table 1 Correlation coefficients between [CO], CDOM optical parameters, DOC, Chl-*a*, O_2, salinity, and temperature in SSW a) and SML b).

a)

	$[CO]_{ssw}$	Temperature	Salinity	O_2	$a_{CDOM}(254)$	$a_{CDOM}(330)$	$a_{CDOM}(355)$	C1	C2	C3	DOC	Chl-*a*	$SUVA_{254}$	$S_{275-295}$	$S_{350-400}$
Temperature	-0.001														
Salinity	0.017	0.699**													
O_2	-0.072	-0.977**	-0.723**												
$a_{CDOM}(254)$	-0.029	-0.907**	**-0.716****	0.876**											
$a_{CDOM}(330)$	-0.118	-0.783**	**-0.690****	0.758**	0.939**										
$a_{CDOM}(355)$	-0.151	-0.717**	**-0.622****	0.690**	0.894**	0.990**									
C1	0.008	-0.591**	**-0.758****	0.596**	**0.675****	0.680**	0.632**								
C2	0.053	-0.324*	**-0.341****	0.286*	**0.533****	0.592**	0.599**	0.759**							
C3	-0.049	-0.788**	**-0.851****	0.779**	**0.894****	0.887**	0.838**	0.891**	0.665**						
DOC	0.008	-0.598**	-0.239	0.583**	**0.532****	0.394**	0.354**	0.241	0.146	0.323*					
Chl-*a*	0.109	-0.357**	-0.092	0.415**	**0.333****	0.235	0.208	0.104	0.159	0.215	0.348**				
$SUVA_{254}$	-0.081	-0.676**	-0.705**	0.654**	**0.824****	**0.860****	**0.831****	**0.653****	**0.560****	**0.853****	-0.006	0.134			
$S_{275-295}$	0.045	0.100	0.099	-0.092	-0.204	-0.385**	-0.448**	-0.197	-0.241	-0.269*	-0.009	0.084	-0.241		
$S_{350-400}$	-0.001	0.009	-0.060	0.044	-0.095	-0.214	-0.279*	0.009	-0.103	-0.043	-0.088	0.026	-0.050	0.867**	
S_R	0.059	0.346**	0.421**	-0.429**	-0.254*	-0.220	-0.134	-0.343**	-0.104	-0.393**	-0.087	-0.148	-0.316*	-0.506**	-0.645**

*Correlation is significant at the 0.05 level (two-tailed).

**Correlation is significant at the 0.01 level (two-tailed). N = 44.

b)

	$[CO]_{sml}$	Temperature	Salinity	SML $a_{CDOM}(254)$	SML $a_{CDOM}(330)$	SML $a_{CDOM}(355)$	SML C1	SML C2	SML C3	SML DOC	SML $SUVA_{254}$	SML $S_{275-295}$	SML $S_{350-400}$
Temperature	-0.032												
Salinity	-0.098	0.699**											
SML $a_{CDOM}(254)$	-0.137	-0.037	-0.045										
SML $a_{CDOM}(330)$	-0.119	-0.113	-0.135	**0.948****									
SML $a_{CDOM}(355)$	-0.143	-0.114	-0.146	**0.901****	0.989**								
SML C1	-0.095	0.158	-0.156	**0.711****	0.504**	0.434**							
SML C2	-0.217	0.089	-0.106	**0.670****	0.675**	0.673**	0.702**						
SML C3	-0.060	0.092	-0.154	**0.823****	0.622**	0.541**	0.938**	0.703**					
SML DOC	-0.018	0.136	0.174	**0.898****	0.783**	0.705**	0.572**	0.280	0.665**				
SML $SUVA_{254}$	-0.063	-0.250	-0.439**	0.136	0.303*	0.376**	0.240	**0.501****	0.262	-0.272			
SML $S_{275-295}$	0.254	0.241	0.223	0.040	-0.217	-0.318*	0.323*	-0.056	0.336*	0.216	-0.409**		
SML $S_{350-400}$	0.270	0.112	0.082	0.136	-0.090	-0.187	0.385**	0.047	0.427**	0.244	-0.281	0.968**	
SML S_R	-0.288	0.231	0.213	-0.248	-0.057	0.044	-0.276	0.029	-0.339*	-0.296*	0.167	-0.726**	-0.776**

*Correlation is significant at the 0.05 level (two-tailed).

**Correlation is significant at the 0.01 level (two-tailed). N = 44.

Table 2 Correlation coefficients between EFs of CO, DOM absorption, DOC, three fluorescence components, temperature, salinity, and wind speed.

	EF of CO	EF of DOC	EF of $a_{CDOM}(254)$	EF of $a_{CDOM}(330)$	EF of $a_{CDOM}(355)$	EF of C1	EF of C2	EF of C3	Temperature	Salinity	Wind speed
EF of DOC	-0.098										
EF of $a_{CDOM}(254)$	-0.067	0.867**									
EF of $a_{CDOM}(330)$	-0.111	0.726**	0.912**								
EF of $a_{CDOM}(355)$	-0.124	0.556**	0.752**	0.945**							
EF of C1	0.081	0.731**	0.898**	0.753**	0.619**						
EF of C2	-0.084	0.149	0.586**	0.600**	0.580**	0.486**					
EF of C3	-0.022	0.796**	0.935**	0.830**	0.714**	0.964**	0.502**				
Temperature	0.037	**0.363****	**0.528****	**0.533****	**0.456****	**0.617****	**0.296***	**0.604****			
Salinity	0.006	**0.289***	**0.478****	**0.493****	**0.427****	**0.500****	**0.268**	**0.491****	0.699**		
Wind speed	-0.177	0.008	0.186	0.159	0.161	-0.130	-0.006	-0.105	0.129	0.052	
Solar irradiance	**0.409****	-0.024	-0.051	-0.082	-0.050	0.022	-0.139	0.002	0.160	0.157	0.104

*Correlation is significant at the 0.05 level (two-tailed).

**Correlation is significant at the 0.01 level (two-tailed). N = 44.

cc

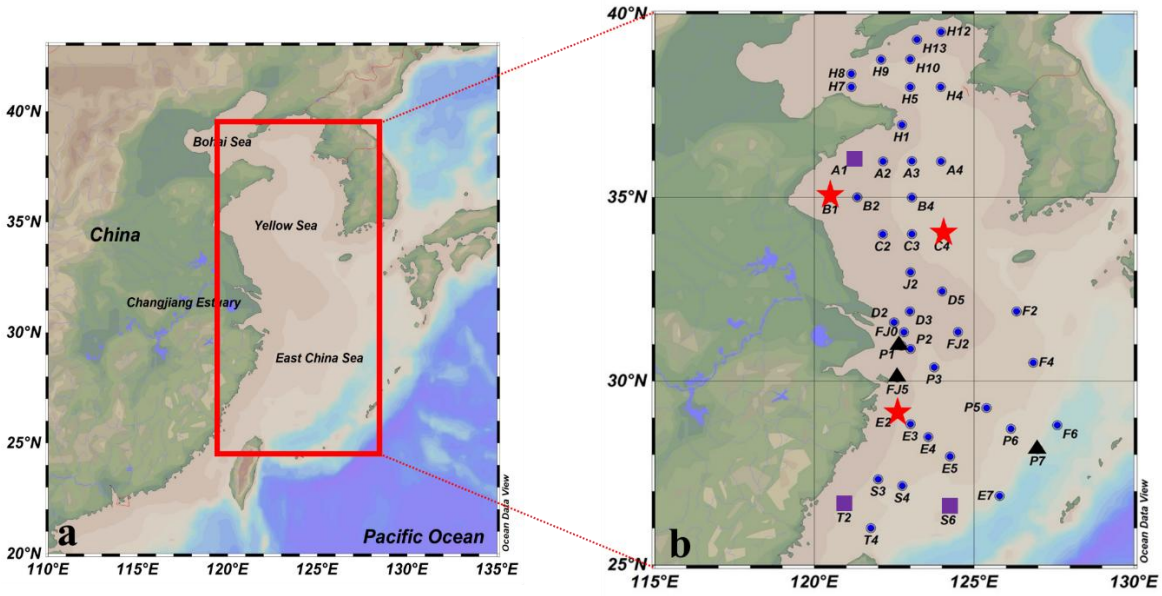

Fig. 1 Map of sampling stations in the East China Sea and the Yellow Sea during winter. Red box represented photochemical incubation experiment stations, and the purple rhomboid represented biological consumption experiment stations.

■: Stations for CO microbial consumption incubation experiments; ▲: Stations for CO photochemical production incubation experiments; ★: Station for both CO microbial consumption and photochemical production incubation experiments; ●: Stations only for seawater sampling.

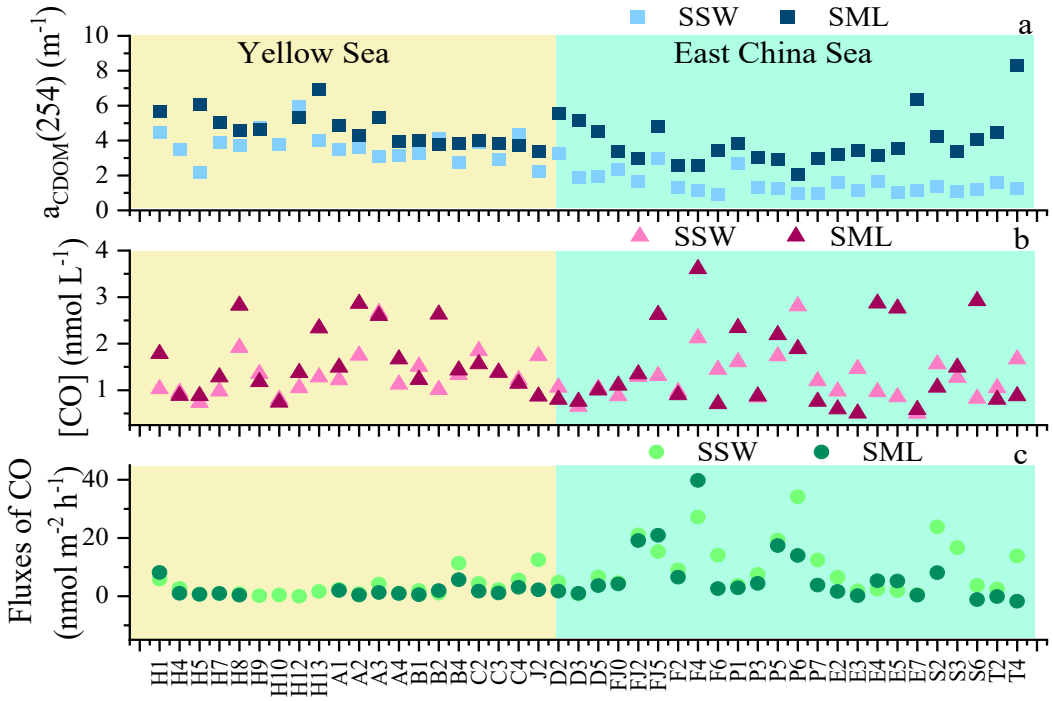

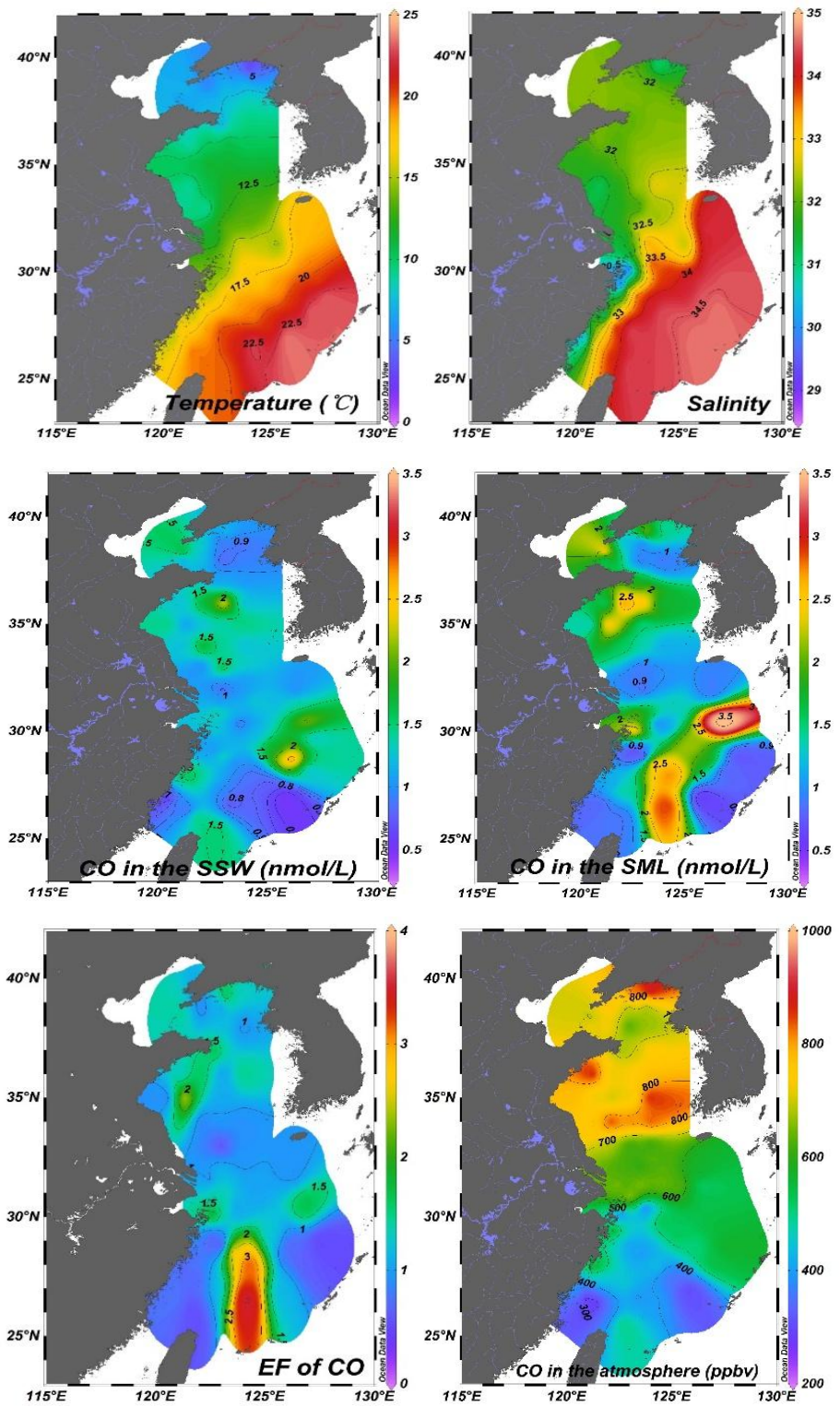
Temperature (℃)
Salinity
CO in the SSW (nmol/L)
CO in the SML (nmol/L)
EF of CO
CO in the atmosphere (ppbv)
40°N
35°N
30°N
25°N
115°E
120°E
125°E
130°E
Ocean Data View

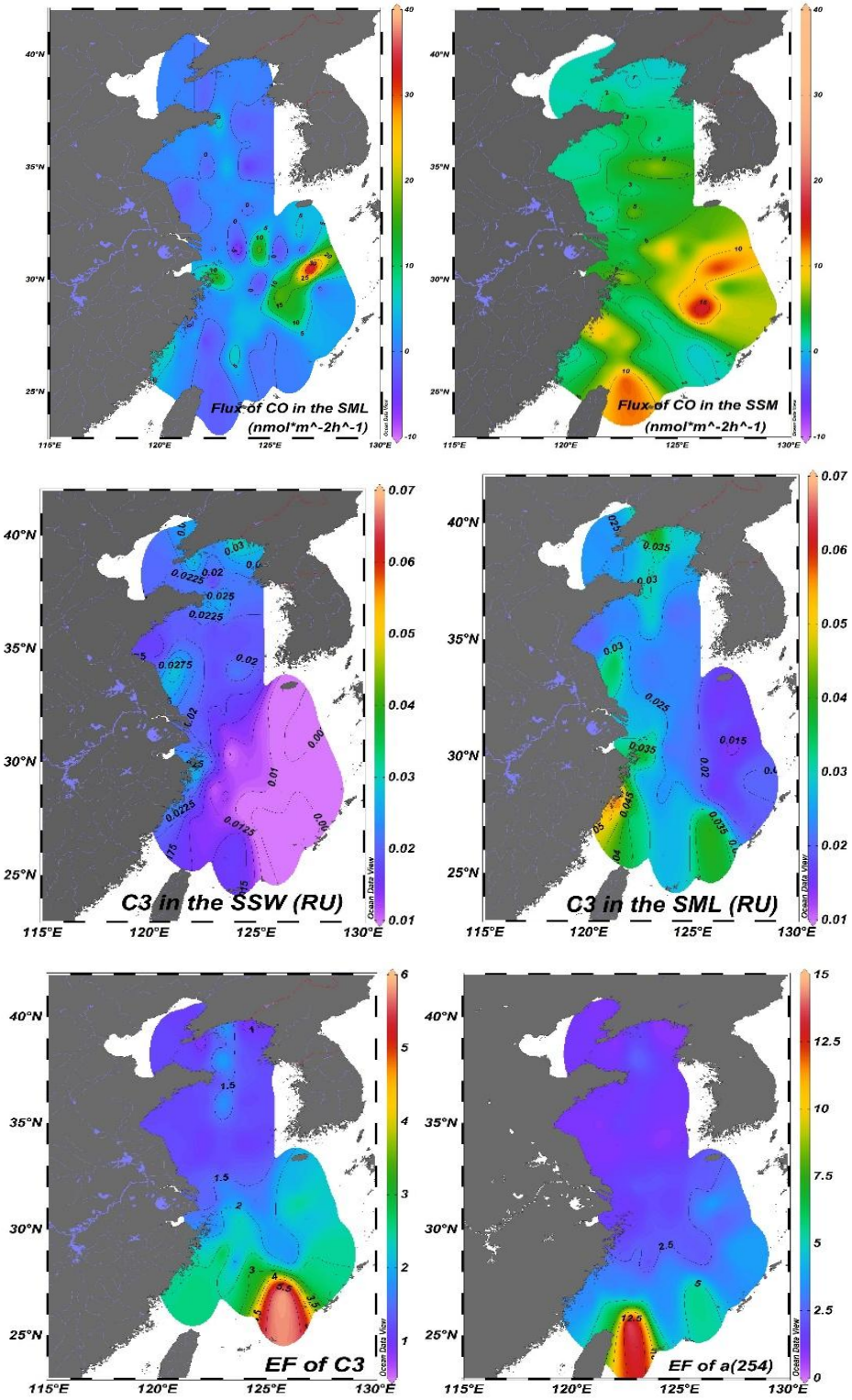

Fig. 2 $a_{CDOM}(254)$ values in the SSW and the SML (a); CO concentrations in the SSW and the SML (b); The flux of CO in the SSW and the SML (c); Spatial distributions of temperature and salinity, CO and the marine-like fluorescence C3 in the SSW and the SML; CO in the atmosphere, and the enrichment factors of CO and the marine-like fluorescence C3 in the SML in the East China Sea and the Yellow Sea in January 2020

(d). The concentration profiles of CO in the SSW resemble those of CO in the SML, which is evidence for a biogeochemically very stable environment.

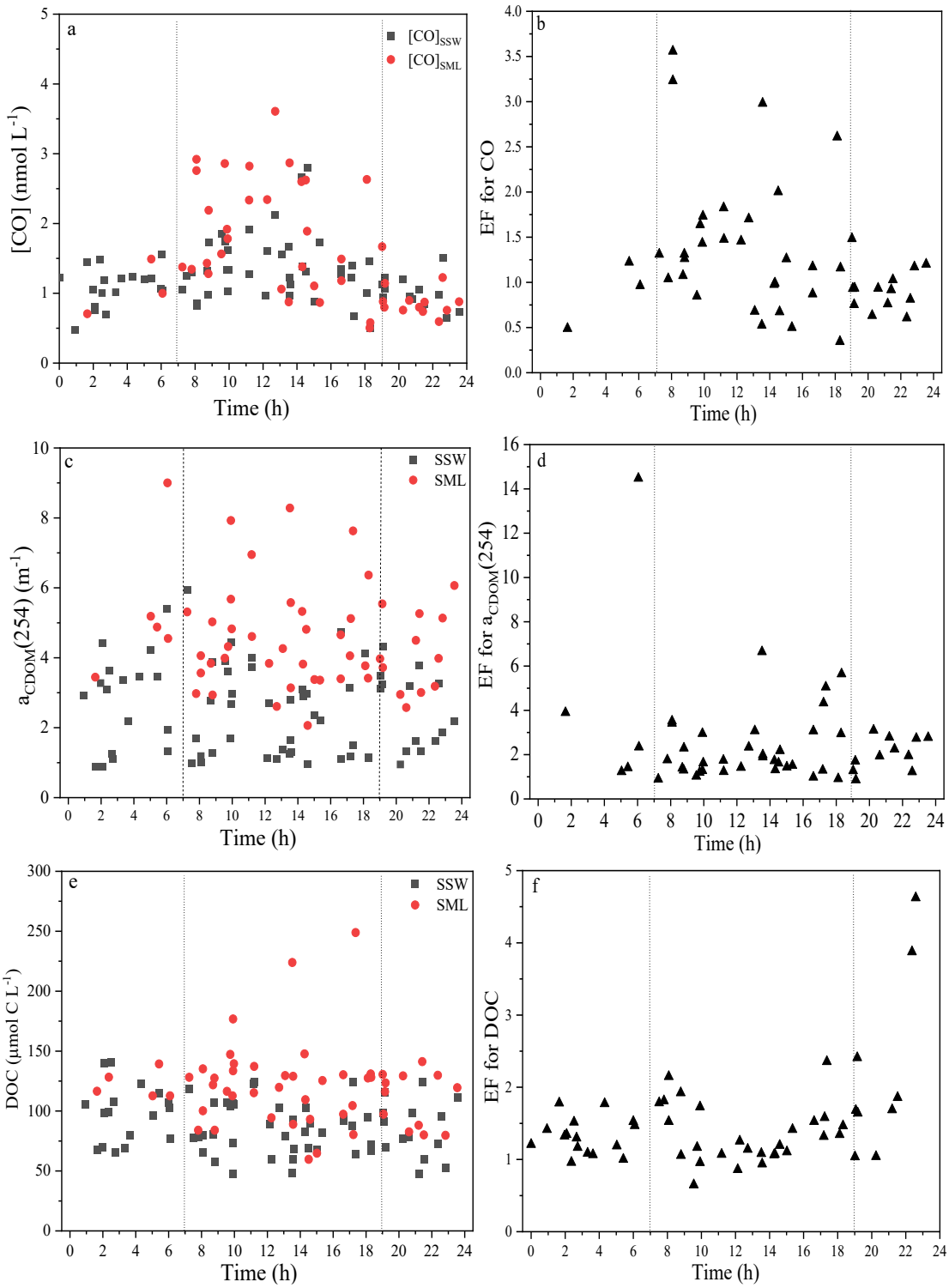

Fig. 3 Variations in the $[CO]_{SML}$, $[CO]_{SSW}$, $a_{CDOM}(254)$, and DOC, EFs of [CO], $a_{CDOM}(254)$, and DOC with the sampling time at each station.

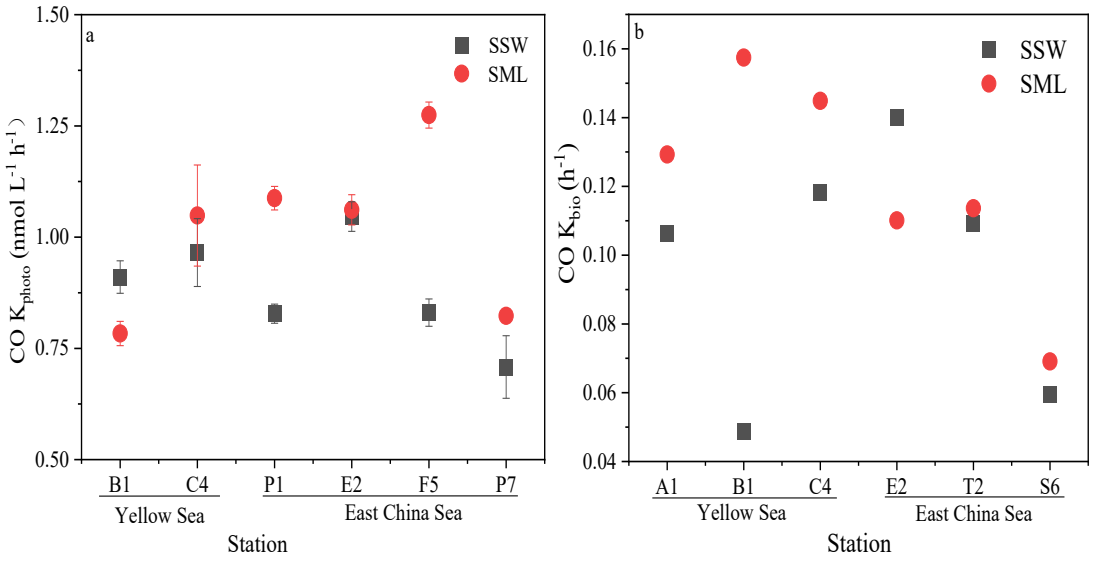

Fig. 4 Variations in photochemical CO production rate of CO (K_{photo}) in the SML (red) and the SSW (black) (a)). Variations in microbial consumption rate constants of CO (K_{bio}) in the SML (red) and the SSW (black). Data are presented as mean values and error bars represent the standard deviation of duplicate samples.

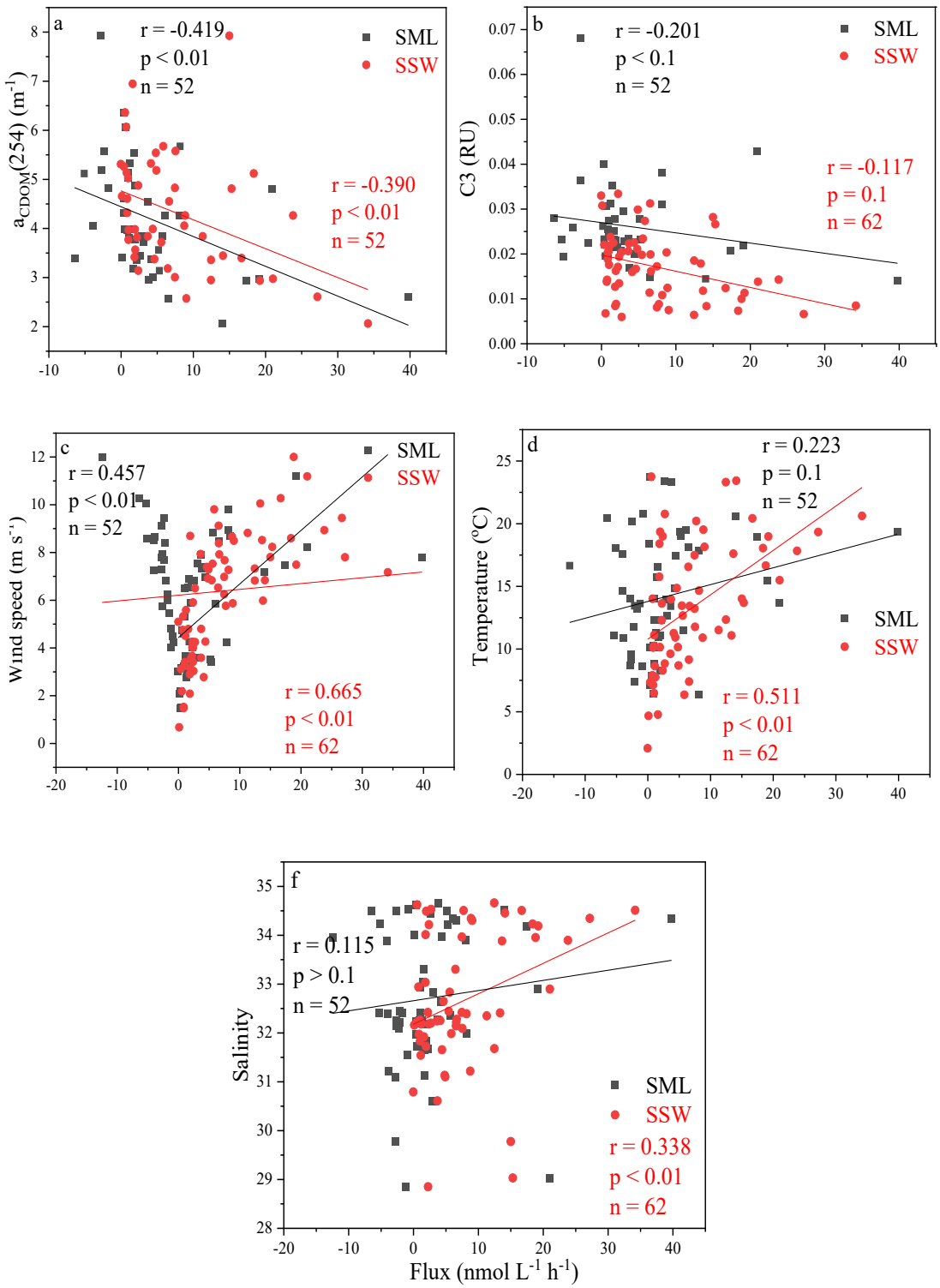

Fig. 5 Correlations between the instantaneous sea-to-air fluxes of CO (Flux) in the SSW and the SML with $a_{CDOM}(254)$, marine humic-like C3, wind speeds, temperature, and salinity in the East China Sea and the Yellow Sea during winter.

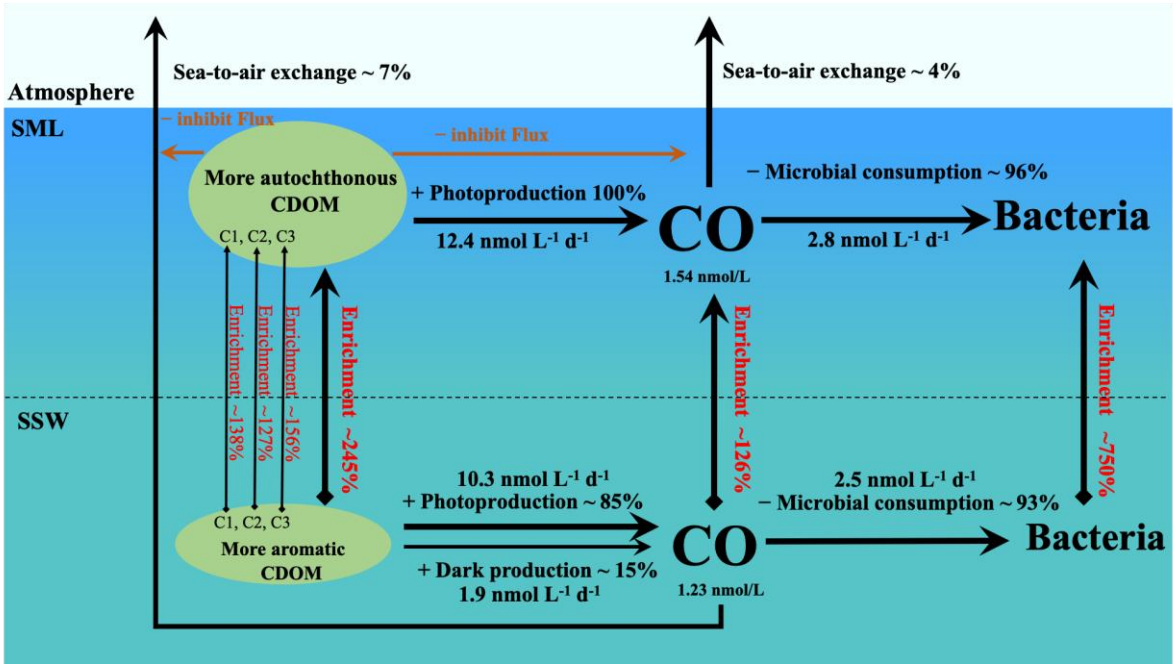

Fig. 6 Budget model of CO transformation in the SML and the SSW in the eastern marginal seas of China during winter. (Bacterial enrichment was calculated by Sun et al., 2020).